Shortwave radiative flux variability through the lens of the Pacific Decadal Oscillation

Boriana Chtirkova[1], **Doris Folini**[1], **Lucas Ferreira Correa**[1], **Martin Wild**[1]

[1]Institute for Atmospheric and Climate Sciences, ETH Zürich, Zürich, Switzerland

Key Points:

- The PDO is a prominent pacemaker for variability, accounting for about 1/3 of the shortwave flux year-to-year variability over NH continents.
- A negative PDO anomaly leads to a reduction in atmospheric shortwave reflectivity (clouds) in North America and Europe and an increase in India.
- The redistribution of clouds in response to a North Pacific PDO anomaly might influence SSTs in the South Pacific and North Atlantic.

Corresponding author: Boriana Chtirkova, boriana.chtirkova@env.ethz.ch

Abstract

The variability of the shortwave radiative fluxes at the surface and top of atmosphere (TOA) is examined in a pre-industrial modelling setup using the Pacific Decadal Oscillation (PDO) as a possible pacemaker of atmospheric decadal-scale variability. Within models from the Coupled Model Intercomparison Project – Phase 6, downwelling shortwave radiation at the surface, the net shortwave fluxes at the surface and TOA, as well as cloud radiative effects show remarkably similar patterns associated with the PDO. Through ensemble simulations designed with a pure PDO pattern in the North Pacific only, we show that the PDO relates to about 20-40% of the unforced year-to-year variability of these shortwave fluxes over the Northern Hemispheric continents. The SST imprint on shortwave-flux variability over land is larger for spatially aggregated time series as compared to smaller areas, due to the blurring effect of small-scale atmospheric noise. The surface and TOA radiative flux anomalies associated with the PDO index range of $[-1.64; 1.64]$ are estimated to reach up to ± 6 Wm^{-2} for North America, ∓ 3 Wm^{-2} for India and ± 2 Wm^{-2} for Europe. We hypothesise that the redistribution of clouds in response to a North Pacific PDO anomaly can impact the South Pacific and North Atlantic SSTs.

Plain Language Summary

We investigate how solar radiation at Earth's surface and the top of the atmosphere, which are mainly controlled by cloudiness, can vary over decades as a response to a horseshoe pattern typical for the North Pacific sea surface temperatures (SSTs) – the Pacific Decadal Oscillation (PDO). We use idealized climate model simulations to show that about a third of the year-to-year changes in solar radiation over the Northern Hemispheric continents are related to this phenomenon. These changes are more noticeable when looking at large areas rather than small ones, as high frequency smaller scale atmospheric variations can obscure the bigger picture. By keeping the PDO fixed to a constant negative value, implying below average cold sea surface temperatures off the western coast of North America and warmer than average temperatures towards Japan, we show that North America and Europe exhibit a reduction in cloudiness, while clouds increase in India.The same with an opposite sign is true for a positive PDO anomaly. These changes in cloud patterns might further affect SSTs in the South Pacific and North Atlantic oceans.

1 Introduction

Internal climate variability on a range of spatial and temporal scales and its interplay with radiative processes is important for understanding Earth's energy balance and its potential response to changing forcings over different temporal and spatial scales. The shortwave part of Earth's energy budget, specifically absorbed solar radiation (or net shortwave flux at the top of atmosphere, TOA) and its response to greenhouse gas forcing are shown to be fundamental for Earth's climate and climate change (Trenberth & Fasullo, 2009; Donohoe et al., 2014). From a surface perspective, aerosols and their temporal variability are suggested to impact the surface energy balance by altering downwelling shortwave radiation at the surface (e.g. Stanhill and Moreshet (1992); Wild (2009); Wild et al. (2012, 2014)).

Several studies have shown that internal climate variability interferes with the energy fluxes on a range of scales, notably including decadal time scales at TOA (e.g. Allan et al. (2014); Loeb et al. (2018, 2021); Wills et al. (2021); Meyssignac et al. (2023)) and at the surface (e.g. Folini et al. (2017); Augustine and Capotondi (2022); Chtirkova et al. (2023)). Variations are shown to relate to known elements of internal variability like El Niño–Southern Oscillation (ENSO), Pacific Decadal Oscillation (PDO), Atlantic Multidecadal Oscillation (AMO). The focus of our study is the PDO, which is identified as the dominant pattern of sea surface temperature variability in the North Pacific, characterised by decadal-scale warming and cooling with a characteristic horseshoe pattern

(Mantua & Hare, 2002). Over decadal time scales, the PDO is associated with strengthening and expansion of the North Pacific subpolar gyre in response to a deepening of the Aleutian Low and increasing variability at longer time scales due to adjustment of westward propagating oceanic Rossby waves (Qiu et al., 2007; Taguchi et al., 2007; Wills et al., 2019)). The PDO has a South Pacific counterpart, referred to as South Pacific Decadal Oscillation (SPDO, Chen and Wallace (2015); IPCC (2021)), which is thought to be influenced by a collection of processes including extratropical modes, ENSO teleconnections and ocean dynamics (Shakun & Shaman, 2009; Zhang et al., 2018). The combined phenomenon between PDO, ENSO and SPDO, though believed to be physically distinct modes (Newman et al., 2016; IPCC, 2021), is the Inter-decadal Pacific Oscillation (IPO, Power et al. (1999); Folland (2002); Henley et al. (2015)).

The PDO is found to be related to atmospheric dynamics, specifically the Pacific North American pattern, and is strongly correlated with temperature and precipitation patterns over North America (Liu et al., 2017; Rohli et al., 2022). There are further indications of a possible link between the Pacific North American Pattern and North Atlantic Oscillation and Atlantic storm tracks trough baroclinic waves (Pinto et al., 2010). The PDO has also been proposed as the major driver of decadal-scale surface downwelling shortwave radiation anomalies (dimming and brightening) for the United States (Augustine & Capotondi, 2022) and is also hypothesised as a contributor to European dimming and brightening (Chtirkova et al., 2023).

In this study, we focus on various aspects of the shortwave part of Earth's energy budget, including the downwelling shortwave radiation at the surface – $F_S^{\downarrow}$, net shortwave radiation at the top of the atmosphere (TOA, positive downward) – $F_T^{\downarrow\uparrow}$, net shortwave radiation at Earth's surface (positive downward) – $F_S^{\downarrow\uparrow}$, shortwave atmospheric absorption – A_{atm}, and the shortwave cloud radiative effects at the surface and TOA – CRE_S, CRE_T. As our interest is with the PDO as a potential pacemaker of part of the internal variability of shortwave fluxes for decadal scales, we use the PDO evolution as a reference and examine the shortwave fluxes "through the lens of the PDO". We do so by analysing both coupled climate model simulations from the Coupled model intercomparison project – Phase 6 (CMIP6, Eyring et al. (2016)) and our own simulations with the atmosphere-only global climate model ICON, where we constrain the PDO spatial anomaly to a specific value and assess the response of the shortwave radiative fluxes. The paper is structured as follows: in section 2 we describe the data and experimental setup. The results are presented in three parts: in section 3.1, we identify patterns of decadal trends in the shortwave fluxes; in section 3.2, we estimate the fraction of total variability attributable to SSTs and PDO and in section 3.3 we quantify the anomalies in the radiative fluxes as a function of the PDO index value. In section 4, we discuss potential differences that arise from the lack of coupling or from using specifically ICON-A, we also bring observed PDO anomalies into the picture. We conclude in section 5.

2 Data and Methods

The study consists of two parts – we use coupled model data to pinpoint the qualitative relationship between the SW fluxes and PDO and we give a quantification of the fraction of variability attributable to PDO and the flux anomalies in Wm^{-2} based on our own numerical simulations.

2.1 CMIP6 Data

The first part of the study uses the unforced control simulations (piControl) of CMIP6 (Eyring et al., 2016) to investigate the unforced variability of the shortwave fluxes at the surface and TOA and relate them to the PDO. The PDO index for the CMIP6 analysis is computed using the the Climate Variability Diagnostics Package—CVDP, version 5.1.1 (Phillips et al., 2014), developed by NCAR's Climate Analysis Section. We include

52 simulations from 44 coupled models. The multiple simulations for some models come from slightly modified model versions in terms of physical parameterizations used or as different realizations. The full list is given in Table 1. Our analysis uses annual mean data, and is performed on a per grid box level. The radiative fluxes are interpolated to a 1°grid (same as the GFDL-ESM4 grid) using 2nd order conservative remapping. This part is an expansion of Chtirkova et al. (2023) to all short shortwave fluxes: for each of the 52 simulations, we use annual mean data to compute the distribution of all possible trends (linear regressions) in the PDO index, then we take the periods with trend magnitudes below the 10th and above the 90th percentile and combine them into composite (mean) trend maps of the shortwave fluxes – one for the increasing and one for the decreasing phases of the PDO, subsequently combining individual models into multimodel median maps, one per shortwave flux component. In addition, to provide a region specific discussion, we select four regions by visual inspection of the shortwave flux trend maps (that are derived from PDO index trends), focusing on regions that do show trends upon strong changes of the PDO. We choose regions with approximately equal area (between 3.7 and 3.9 10^6 km^2). The regions we come up are the following and we refer to them with the names of the nearest (but not the whole) geographical features they cover: North America (30-50°N, 250-270°E), Europe (40-55°N, 0-30°E), India and Indochinese Peninsula (10-18°N, 71-110°E) and Australia (15-30°S, 128-150°E). A visual depiction of the regions is provided on the last subplot of Figure 2.

2.2 ICON-A simulations

We use the atmospheric part of the icosahedral nonhydrostatic (ICON) Earth System Model (ESM): ICON-A (Jungclaus et al., 2022). The atmospheric general circulation model ICON-A (Giorgetta et al., 2018; Crueger et al., 2018) is in a configuration using the Max Planck Institute climate physics package and the rotated R2B4 grid (grid id 0013), the same as in the ICON-ESM-LR CMIP6 data with an approximate grid increment of 160 km. The tuning configuration is also the same as in the coupled version's piControl simulation. As boundary conditions, we use monthly mean SST data from the first 100 (out of 500) years coupled simulation within CMIP6. The SST climatological mean fields for the simulations as well as sea ice climatologies are computed over all 500-years of ICON-ESM-LR data. All other boundary conditions are kept at pre-industrial climatological values, including sea ice data, stratospheric ozone and aerosol optical properties. Well-mixed greenhouse gasses have a constant vertical mixing ratio and the solar constant is kept at 1360.744 Wm^{-2} in accordance with CMIP6 protocols. Our motivation for using SST data from the coupled CMIP6 run instead of observed data is twofold: (1) we have 500 years of statistics that are not contaminated by global warming and (2) the SST field is in part characteristic of the atmospheric circulation. By using SSTs from the coupled counterpart of the same model, we avoid a possible mismatch between the SST data and the specifics of the atmospheric circulation of the ICON model its R2B4 grid.

We run experiments with prescribed SSTs, where we retain only the low-frequency component of the PDO. This is done by first decomposing the SST field (500-years of ICON-ESM-LR) into eigenvectors (empirical orthogonal functions, EOFs), eigenvalues and their principal components (PCs). Following the recommendations of NCAR Climate Data Guide (Schneider et al., 2013), we deseasonalize and decompose the SST field in a rectangular box in the North Pacific. The box boundaries are taken from the CVDP source code (which we use for the CMIP6 analysis). The EOF decomposition is done using the Python package: pyEOF (Zheng, 2021), which uses the Numpy singular value decomposition methods (Harris et al., 2020). The PDO is defined as the first principal component (PC$_1$, the one with the largest eigenvalue) of the decomposed field – Figure 1 shows the eigenvector expressed as correlation (a), its corresponding time series (b) and power spectra (c). We further low-pass filter the principal component time series using a logarithmic function in frequency space with a time window of 10 years. To obtain a

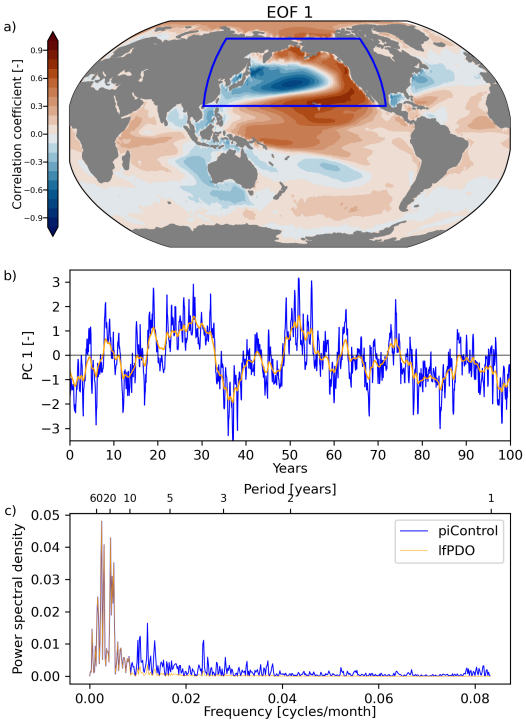

Figure 1. First eigenvector and PC time series derived from EOF analysis of the SST field in ICON-ESM-LR's piControl run. The first EOF (eigenvector), shown in (a), is presented as the correlation with the monthly SST time series for each grid box. Blue box shows the region in which the EOF decomposition is done. In (b), the normalized value of the original first PC (PDO index) time series is displayed in blue and its low-pass filtered counterpart in orange. Shown are only the first 100 years. Low pass filtering is done by smoothing out frequencies of larger than 1/10 years with a sharp logarithmic function. Panel (c) displays the power spectral density estimated using Welch's method (Welch, 1967) for the entire 500-year simulation.

complete SST field as model boundary conditions, we re-project the resulting low-frequency time series (lfPDO) on the PDO eigenvector and add the per-grid box seasonal cycle on top. We do not sum up the remaining eigenvectors and principal components, giving us an SST field, where the only inter-annual variability comes from the PDO pattern. All grid boxes outside the PDO box are kept at their climatological values, apart from a smoothing distance around the box which is included for numerical considerations and detailed in the Appendix Appendix A.

To better carve out variability related to SST variability in general and SST variability related to the PDO in particular, we run two main sets of simulations with 20 ensemble members each: a set of 100-year simulations where the SST field is taken as is from the first 100-years of the piControl run ("allSST") and another set of 100-year simulations where the only variability in the SST field comes from the low frequency component of the PDO obtained as described above via low-pass filtering and projecting the PC_1 time series ("lfPDO"). Ensemble members share the initialization of the atmosphere but differ in the calendar day and associated insulation at simulation start (e.g. January 1, January 5 etc.). We discard the first 1-5 years after initialization, considering this as model spin up, and analyze only subsequent data. This data corresponds to simulation years 4006-4099 of the ICON-ESM-LR piControl run (95 years in total).

To further quantify the influence of a concrete PDO phase (index value) on the SW fluxes, we run seven 100-year simulations with a "perpetual" PDO phase with different amplitudes of the SST anomaly and analyse the last 95-years to reduce the impact of the initial condition. To obtain the field, we take the 99^{th}, 95^{th} and 68^{th} percentiles of the distribution of monthly PDO index values from the 500-year ICON-ESM-LR CMIP6 piControl simulation, and project constant time series with these index values onto the PDO eigenvector, seasonality is added on top. The seven PDO index values we consider based on the above mentioned percentiles and their negative counterparts are 2.58, 1.64, 0.44, 0, -0.44, -1.64 and -2.58. SST anomalies that correspond to these values are further detailed in the Appendix Appendix A.

3 Results

We examine the impact of the PDO on the various shortwave flux components. Each subsection takes a different perspective in terms of time scales (decadal scale trends and year-to-year variability) and with regard to the details of the PDO. Section 3.1 looks at the PDO arising in fully coupled CMIP6 piControl simulations, where it combines with other modes of variability, and asks about the imprint of strong PDO phase changes on decadal scale trends of the various shortwave fluxes. Sections 3.2 and 3.3, by contrast, look at a PDO the pattern of which is highly idealized by design, comprising only the North Pacific region. Associated atmosphere-only simulations with the ICON-A model are used to examine the imprint of this idealized PDO on shortwave fluxes: how the year-to-year variability of the PDO mirrors in shortwave flux time series (3.2) and how shortwave fluxes differ between ever-lasting positive and negative PDO phases, respectively (3.3). The latter experiments offer an idealized view on strong PDO phase changes.

3.1 Patterns related to PDO

Our first quest is to investigate the patterns of the shortwave radiative flux components related to PDO phase shifts within CMIP6 models. The analysis is done for the distribution of all possible 20-year trends (linear regressions) of the PDO index, selecting the periods with strongest transitioning of the index and computing the trends of the energy balance components for those periods (same as in Chtirkova et al. (2023) for $F_S^{\downarrow}$). The strongest transitions of the PDO index in our case correspond to 20-year trends above 90^{th} and below 10^{th} percentiles for PDO↑ and PDO↓ transitions respectively. The results are presented in Figures 2 and 3. For simplicity, we only discuss results related to PDO↑ in the text, i.e. the PDO changing phase from negative to positive, bearing in mind that the same is valid with opposite sign for the opposite transition.

For the all-sky shortwave fluxes, we find that the patterns are remarkably similar both in spatial structure and in magnitude for $F_S^{\downarrow}$ and the net shortwave fluxes at the surface and TOA ($F_S^{\downarrow\uparrow}$, $F_T^{\downarrow\uparrow}$). This suggest that the reduction of $F_S^{\downarrow}$ (in N. America and Europe during PDO↑) is also associated with a reduction in $F_T^{\downarrow\uparrow}$ and in $F_S^{\downarrow\uparrow}$, i.e. less shortwave radiation absorbed over these regions by the whole system and in particular – at Earth's surface. A significantly different pattern is displayed by shortwave atmospheric absorption (A_{atm}). Regions bearing a statistically significant imprint (no hatching) of the PDO phase shift in A_{atm} may not show up in the other shortwave fluxes and vice versa (e.g. parts of Africa or the Americas). Regions featuring a statistically significant impact from PDO phase changes may show opposite signs for A_{atm} than for the other shortwave fluxes. This is notably the case in wide parts of the Pacific and neighbouring regions. For example, the increase in $F_T^{\downarrow\uparrow}$ over Australia combines with a reduction in A_{atm} to result in an even stronger increase in $F_S^{\downarrow}$ downward.

On the clear-sky side (Figure 3), patterns are overall least pronounced for $F_{T,cs}^{\downarrow\uparrow}$. The much more pronounced and geographically more extended patterns in $F_{S,cs}^{\downarrow}$ and $A_{\text{atm,cs}}$

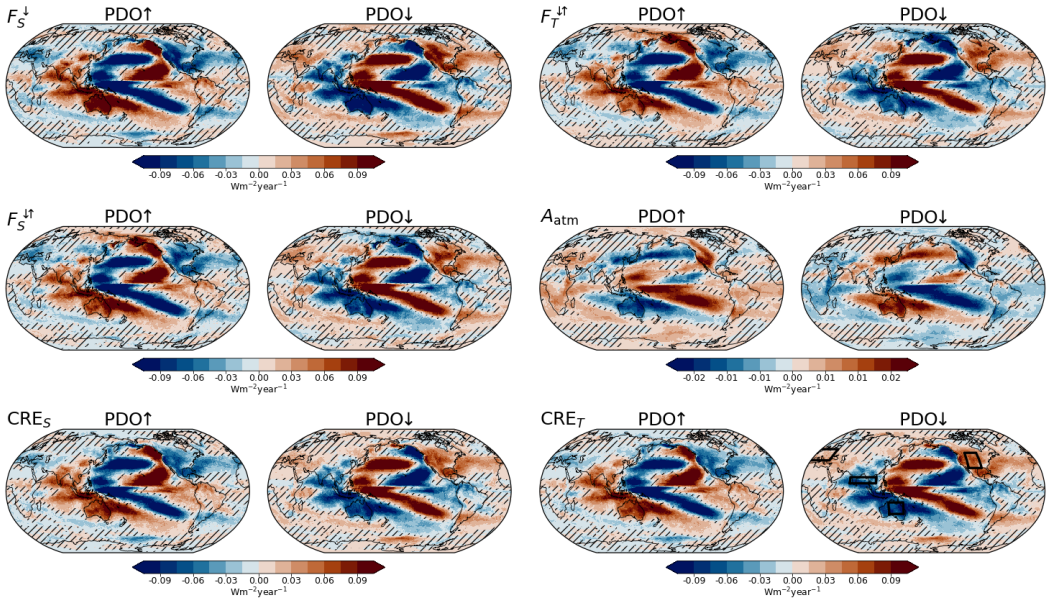

Figure 2. All-sky shortwave flux and cloud radiative effect trend patterns during 20-year periods with a strong negative-to-positive phase transition of the PDO index (PDO↑) and periods with a strong positive-to-negative transition (PDO↓) obtained from CMIP6 piControl simulations. Each map is composed of radiative flux trends which correspond the strongest 10% trends in the PDO index, averaged for each CMIP6 model. Multi-model median is computed among the maps obtained from 52 CMIP6 piControl simulations. Hatched regions represent areas where the Mann-Whitney-U test is passed at the 0.05 confidence level, i.e. differences between the distributions built from individual models for the PDO↑ and PDO↓ periods at that grid box are not statistically significant. Black boxes on the last map are those, over which we compute aggregated time series.

follow each other closely but with opposite sign, suggesting that changes in $F_{S,cs}^{\downarrow}$ are primarily mediated by changes in $A_{\text{atm,cs}}$. The absorbed clear-sky shortwave radiation at the surface ($F_{S,cs}^{\downarrow\uparrow}$ also resembles the $F_{S,cs}^{\downarrow}$ and $A_{\text{atm,cs}}$ for most ocean areas except for the parts where sea ice plays a role. The clear-sky $F_{T,cs}^{\downarrow\uparrow}$ in the Arctic regions increases with PDO↑, which is associated with less reflectivity in the system, likely due to the decreased sea ice area during a warm PDO (Simon et al., 2022).

This surface albedo effect is also evident in the all-sky patterns. The difference in the all-sky A_{atm} and clear-sky $A_{\text{atm,cs}}$ implies that increased absorption in cloudy conditions due to multiple scattering is significant for regions like the North Pacific.

CREs at the surface and TOA, associated with the different PDO phases, also yield identical patterns and similar magnitudes to $F_S^{\downarrow}$, $F_T^{\downarrow\uparrow}$ and $F_S^{\downarrow\uparrow}$, with the exception of the Arctic. The increase of $F_S^{\downarrow}$, respectively CRE_S (CRE becomes less negative), in the warm North Pacific pool and the decrease in the cold pool (CRE becomes more negative, i.e. more clouds) further serve to enhance the SST anomalies associated with PDO. An interesting feature is the shift from enhanced $F_S^{\downarrow}$, $F_T^{\downarrow\uparrow}$ and $F_S^{\downarrow\uparrow}$ in the warm region during a PDO↑ and the opposite sign trends over North America.

We assess the uncertainty of the presented results on a grid box level in two ways: we test whether the samples assembled upon results from individual models for PDO↑ (first sample) and PDO↓ (second sample) are part of the same distribution using the Mann-

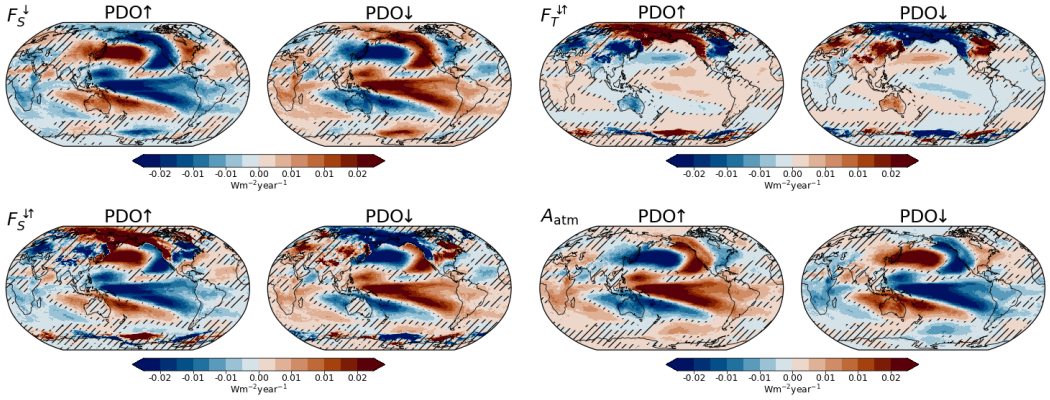

Figure 3. Same as Figure 2 but for the clear-sky fluxes.

Whitney-U test (Mann & Whitney, 1947); we also compute the spread among models (difference between the 90$^{\mathrm{th}}$ percentile and 10$^{\mathrm{th}}$ percentile values) for each grid box. Depending on variable, the Mann-Whitney-U test is passed on the 0.05 level in 27-39% of grid boxes (34% for $F_S^{\downarrow}$), i.e. for these grid boxes there is no statistically significant difference between periods of strongest negative or positive changes in the PDO index. These regions are hatched in Figures 2 and 3. The CMIP6 multi-model spread across grid boxes is on average 0.12Wm^{-2}year^{-1} for the all-sky fluxes and CRE (apart from A_{atm}) and on average 0.02Wm^{-2}year^{-1} for the clear-sky fluxes and all-sky A_{atm} (given are median values across grid boxes representative for all variables). Model spread also depends on the region and is highest in regions where the trend values are the highest. In relative units, the spread in clear-sky fluxes across models is higher in clear-sky as compared to all-sky, which was also highlighted in Chtirkova et al. (2022).

The differences among models with regard to PDO and its relation to shortwave fluxes may be illustrated by inspecting the model specific correlations between the PDO index annual mean time series and regionally averaged annual mean shortwave flux time series, even though they cannot be directly related to the decadal scales discussed above. Corresponding Pearson correlation coefficients are given in Table 1. We choose the four regions (see last map on Figure 2): North America and Europe, where our trend maps show a negative correlation for the all-sky fluxes (apart from A_{atm}) and India and Indochinese Peninsula and Australia where the maps show a positive relationship. For $F_S^{\downarrow}$, $F_T^{\downarrow\uparrow}$ and $F_S^{\downarrow\uparrow}$, almost all models agree on the sign of the relationship in these regions. Exceptions include EC-Earth3, INM-CM4-8, INM-CM5-0 and NorCPM1. Exceptions for A_{atm}, occur more often but trend patterns are also different for A_{atm} as compared to $F_S^{\downarrow}$ and the choice of regions is not optimal for A_{atm}. We also highlight the models which show the strongest correlation coefficients between the PDO index and shortwave fluxes in North America, India and Australia: CESM2-FV2, CESM2-WACCM-FV2, CMCC-CM2-SR5, CMCC-ESM2, GFDL-ESM4, GISS-E2-1-G (p5), ICON-ESM-LR and MIROC6 (given are models showing a correlation coefficient above 0.5 for at least one region and variable). The weaker correlations for Europe are expected due to its larger distance from the Pacific Ocean and other causes for variability there but models still agree on the sign of the relationship.

Going back to trend magnitudes and Figures 2 and 3, we mark as important that even though trend magnitudes are given in absolute units, they are strongly dependent on model and percentile of the PDO index trends over which we select periods. Trend magnitudes are on average 23-28% stronger (depending on variable) when increasing the percentile range from 90-10 (as shown on Figures 2 and 3) to 95-5. This happens for a

Table 1. Pearson correlation coefficients between the annual mean PDO index and all-sky shortwave components of the energy balance: downwelling at surface ($F_S^{\downarrow}$), net at TOA ($F_T^{\downarrow\uparrow}$), net at surface ($F_S^{\downarrow\uparrow}$), and absorbed by the atmosphere (A_{atm}). The SW components are taken as spatially aggregated annual-mean time series for four different regions (drawn on Figure 2). Bold font indicates absolute value of the correlation coefficient larger than or equal to 0.5. Correlation coefficients are calculated over the entire piControl simulations, which yields a different number of years for each model.

	North America				Europe				India and Indochinese Peninsula				Australia			
Model	$F_S^{\downarrow}$	$F_T^{\downarrow\uparrow}$	$F_S^{\downarrow\uparrow}$	A_{atm}	$F_S^{\downarrow}$	$F_T^{\downarrow\uparrow}$	$F_S^{\downarrow\uparrow}$	A_{atm}	$F_S^{\downarrow}$	$F_T^{\downarrow\uparrow}$	$F_S^{\downarrow\uparrow}$	A_{atm}	$F_S^{\downarrow}$	$F_T^{\downarrow\uparrow}$	$F_S^{\downarrow\uparrow}$	A_{atm}
ACCESS-CM2	-0.38	-0.35	-0.36	0.25	-0.16	-0.20	-0.20	0.03	0.22	0.23	0.22	-0.06	0.18	0.19	0.19	-0.15
ACCESS-ESM1-5	-0.42	-0.38	-0.40	0.44	-0.21	-0.22	-0.22	0.16	0.27	0.29	0.26	0.03	0.32	0.31	0.31	-0.28
AWI-CM-1-1-MR	-0.30	-0.27	-0.28	0.24	-0.16	-0.17	-0.17	0.12	0.07	0.06	0.05	0.04	0.27	0.27	0.27	-0.25
BCC-CSM2-MR	-0.26	-0.26	-0.27	0.26	-0.15	-0.16	-0.16	0.13	0.11	0.13	0.11	0.07	0.19	0.18	0.18	-0.14
BCC-ESM1	-0.33	-0.33	-0.35	0.34	-0.10	-0.12	-0.12	0.02	0.00	0.02	0.01	0.14	0.12	0.12	0.12	-0.09
CAS-ESM2-0	-0.49	-0.46	0.03	-0.46	-0.22	-0.24	0.02	-0.24	0.31	0.34	-0.01	0.34	0.35	0.36	-0.03	0.36
CESM2	-0.43	-0.22	-0.27	0.41	-0.19	-0.22	-0.23	0.19	0.38	0.41	0.37	0.07	0.41	0.41	0.34	-0.10
CESM2-FV2	**-0.52**	-0.48	-0.49	0.37	-0.16	-0.18	-0.18	0.13	0.44	0.44	0.43	-0.22	0.49	0.48	0.47	-0.41
CESM2-WACCM	-0.47	-0.25	-0.30	0.46	-0.12	-0.13	-0.15	0.19	0.37	0.39	0.36	-0.02	0.41	0.40	0.35	-0.15
CESM2-WACCM-FV2	**-0.59**	**-0.50**	**-0.52**	**0.50**	-0.19	-0.19	-0.21	0.23	**0.55**	**0.55**	**0.54**	-0.32	0.48	0.49	0.44	-0.20
CIESM	-0.47	-0.28	-0.32	0.43	-0.10	-0.10	-0.10	0.09	0.22	0.25	0.22	-0.01	0.29	0.30	0.29	-0.24
CMCC-CM2-SR5	-0.47	-0.32	-0.35	0.44	-0.20	-0.25	-0.25	0.18	0.46	0.47	0.44	-0.13	**0.52**	**0.50**	**0.51**	**-0.50**
CMCC-ESM2	**-0.51**	-0.37	-0.40	0.44	-0.26	-0.30	-0.31	0.25	**0.54**	**0.54**	**0.52**	-0.23	**0.58**	**0.57**	**0.58**	**-0.56**
CNRM-CM6-1	-0.11	-0.18	-0.19	0.10	-0.11	-0.18	-0.18	0.04	0.16	0.18	0.17	-0.03	0.17	0.18	0.17	-0.14
CNRM-ESM2-1	-0.11	-0.12	-0.13	0.16	-0.11	-0.17	-0.16	0.06	0.22	0.25	0.23	-0.05	0.15	0.16	0.15	-0.13
CanESM5 (p1)	-0.28	-0.14	-0.17	0.16	-0.22	-0.22	-0.22	0.14	0.29	0.33	0.29	-0.06	0.35	0.36	0.35	-0.33
CanESM5 (p2)	-0.23	-0.14	-0.15	0.09	-0.21	-0.24	-0.23	0.12	0.31	0.34	0.31	-0.08	0.35	0.36	0.35	-0.33
CanESM5-CanOE	-0.25	-0.17	-0.18	0.12	-0.20	-0.24	-0.23	0.11	0.33	0.36	0.32	-0.11	0.37	0.37	0.37	-0.36
E3SM-1-0	-0.42	-0.29	-0.33	0.43	-0.12	-0.13	-0.14	0.17	0.15	0.15	0.15	-0.05	0.13	0.15	0.13	-0.06
EC-Earth3	-0.22	-0.24	-0.24	0.15	0.05	-0.17	-0.15	-0.07	0.27	0.27	0.27	-0.21	0.17	0.17	0.17	-0.15
EC-Earth3-CC	-0.38	-0.26	-0.29	0.35	-0.08	-0.23	-0.23	0.14	0.34	0.34	0.33	-0.21	0.28	0.26	0.26	-0.24
FGOALS-f3-L	-0.31	-0.19	-0.22	0.29	-0.21	-0.26	-0.25	0.10	0.17	0.20	0.16	0.08	0.04	0.06	0.05	0.04
FGOALS-g3	-0.18	-0.25	-0.26	0.25	-0.20	-0.31	-0.30	0.19	0.21	0.22	0.21	-0.06	0.24	0.26	0.24	-0.16
GFDL-CM4	-0.38	-0.29	-0.31	0.29	-0.14	-0.18	-0.18	0.05	0.38	0.43	0.38	0.18	0.31	0.33	0.32	-0.23
GFDL-ESM4	**-0.55**	**-0.50**	**-0.52**	0.45	-0.19	-0.18	-0.19	0.13	0.31	0.35	0.29	0.24	0.42	0.42	0.39	-0.08
GISS-E2-1-G (f1)	-0.24	-0.32	-0.31	0.14	-0.31	-0.32	-0.32	0.17	0.46	0.48	0.46	0.05	0.23	0.25	0.23	-0.14
GISS-E2-1-G (f2)	-0.28	-0.33	-0.33	0.24	-0.28	-0.31	-0.31	0.10	0.41	0.44	0.41	0.04	0.26	0.27	0.25	-0.16
GISS-E2-1-G (p3)	-0.28	-0.32	-0.33	0.36	-0.41	-0.42	-0.42	0.28	0.39	0.43	0.39	0.14	0.23	0.25	0.22	-0.12
GISS-E2-1-G (p5)	-0.37	-0.42	-0.43	0.40	-0.40	-0.41	-0.42	0.23	**0.51**	**0.56**	**0.51**	0.30	0.24	0.26	0.23	-0.07
GISS-E2-1-H (f1)	-0.27	-0.28	-0.29	0.23	-0.18	-0.21	-0.20	0.04	0.37	0.39	0.37	-0.01	0.18	0.18	0.18	-0.13
GISS-E2-1-H (f2)	-0.18	-0.19	-0.19	0.12	-0.15	-0.16	-0.15	0.07	0.34	0.35	0.34	-0.03	0.20	0.21	0.20	-0.12
GISS-E2-1-H (p3)	-0.19	-0.17	-0.20	0.31	-0.26	-0.26	-0.26	0.19	0.28	0.30	0.28	0.05	0.17	0.18	0.17	-0.10
HadGEM3-GC31-LL	-0.42	-0.36	-0.38	0.35	-0.21	-0.21	-0.23	0.20	0.32	0.34	0.32	-0.01	0.26	0.30	0.27	-0.14
HadGEM3-GC31-MM	-0.32	-0.22	-0.25	0.25	-0.16	-0.19	-0.20	0.14	0.34	0.34	0.34	-0.14	0.10	0.15	0.10	-0.01
ICON-ESM-LR	**-0.57**	**-0.59**	**-0.58**	0.42	-0.19	-0.22	-0.21	0.12	**0.59**	**0.58**	**0.59**	**-0.51**	0.47	0.46	0.47	-0.48
INM-CM4-8	-0.26	-0.29	-0.28	0.07	-0.08	-0.06	-0.06	0.04	-0.06	-0.06	-0.06	0.08	0.27	0.27	0.27	-0.19
INM-CM5-0	-0.19	-0.25	-0.24	0.05	-0.10	-0.15	-0.14	0.04	-0.15	-0.14	-0.15	0.21	0.02	0.01	0.02	-0.04
IPSL-CM6A-LR	-0.29	-0.30	-0.29	0.16	-0.14	-0.18	-0.18	0.07	0.02	0.05	0.02	0.06	0.28	0.28	0.28	-0.28
KACE-1-0-G	-0.33	-0.17	-0.22	0.34	-0.13	-0.13	-0.15	0.21	0.23	0.24	0.23	-0.03	0.12	0.17	0.12	0.00
MIROC-ES2H	-0.44	-0.33	-0.37	0.45	-0.17	-0.20	-0.20	0.14	0.39	0.44	0.39	0.28	0.32	0.33	0.33	-0.27
MIROC-ES2L	-0.42	-0.35	-0.41	0.49	-0.14	-0.15	-0.16	0.16	0.30	0.41	0.31	0.46	0.20	0.20	0.21	-0.19
MIROC6	**-0.55**	-0.39	-0.44	**0.57**	-0.17	-0.20	-0.21	0.22	0.35	0.41	0.35	0.40	0.39	0.41	0.40	-0.33
MPI-ESM-1-2-HAM	-0.36	-0.35	-0.36	0.29	-0.28	-0.27	-0.27	0.23	0.04	0.06	0.02	0.16	0.27	0.27	0.27	-0.25
MPI-ESM1-2-HR	-0.27	-0.23	-0.24	0.19	-0.21	-0.22	-0.22	0.10	0.14	0.16	0.11	0.14	0.25	0.28	0.26	-0.18
MPI-ESM1-2-LR	-0.42	-0.41	-0.41	0.33	-0.24	-0.25	-0.25	0.22	0.15	0.17	0.13	0.07	0.27	0.28	0.27	-0.22
MRI-ESM2-0	-0.35	-0.20	-0.24	0.33	-0.07	-0.10	-0.09	0.02	0.30	0.35	0.31	0.03	0.18	0.20	0.18	-0.08
NESM3	-0.10	-0.17	-0.12	-0.17	-0.10	-0.12	-0.10	-0.03	0.14	0.13	0.14	-0.13	0.11	0.10	0.11	-0.11
NorCPM1 (r1)	-0.06	0.02	0.00	0.10	-0.24	-0.25	-0.25	0.15	0.25	0.27	0.24	0.13	0.25	0.25	0.24	-0.18
NorCPM1 (r2)	-0.20	-0.17	-0.18	0.20	-0.29	-0.30	-0.29	0.10	0.28	0.29	0.27	0.08	0.32	0.34	0.32	-0.24
NorCPM1 (r3)	-0.12	-0.06	-0.08	0.19	-0.27	-0.26	-0.27	0.20	0.25	0.27	0.24	0.15	0.32	0.32	0.32	-0.26
SAM0-UNICON	-0.46	-0.22	-0.26	0.41	-0.20	-0.20	-0.21	0.18	0.34	0.35	0.34	-0.18	0.49	0.49	0.49	-0.47
UKESM1-0-LL	-0.43	-0.41	-0.44	0.48	-0.19	-0.22	-0.24	0.29	0.27	0.28	0.27	-0.09	0.34	0.37	0.36	-0.29
Median	-0.33	-0.28	-0.29	0.29	-0.19	-0.21	-0.21	0.14	0.30	0.34	0.29	0.03	0.27	0.27	0.27	-0.17

few reasons: (1) PDO trends across models differ and (2) PDO trends in the same model above the 90$^{\text{th}}$ percentile differ, (3) the atmospheric response to the same PDO trend across models might be different. Taking a smaller subset of PDO indices does not necessarily provide better statistics because of too much non-PDO related variability that is not averaged across many data points. To further quantify what fraction of the variability is attributable to the PDO and what are the specific radiative anomalies related to its phases, we rely on results from simplified numerical experiments described in the following sections.

3.2 PDO fraction in variability

In our simplified ICON-A numerical setup, we would firstly like to give an estimate on what fraction of total shortwave flux variability can be attributed to the SST field and what fraction of that is attributable to the PDO pattern. To achieve this, we first

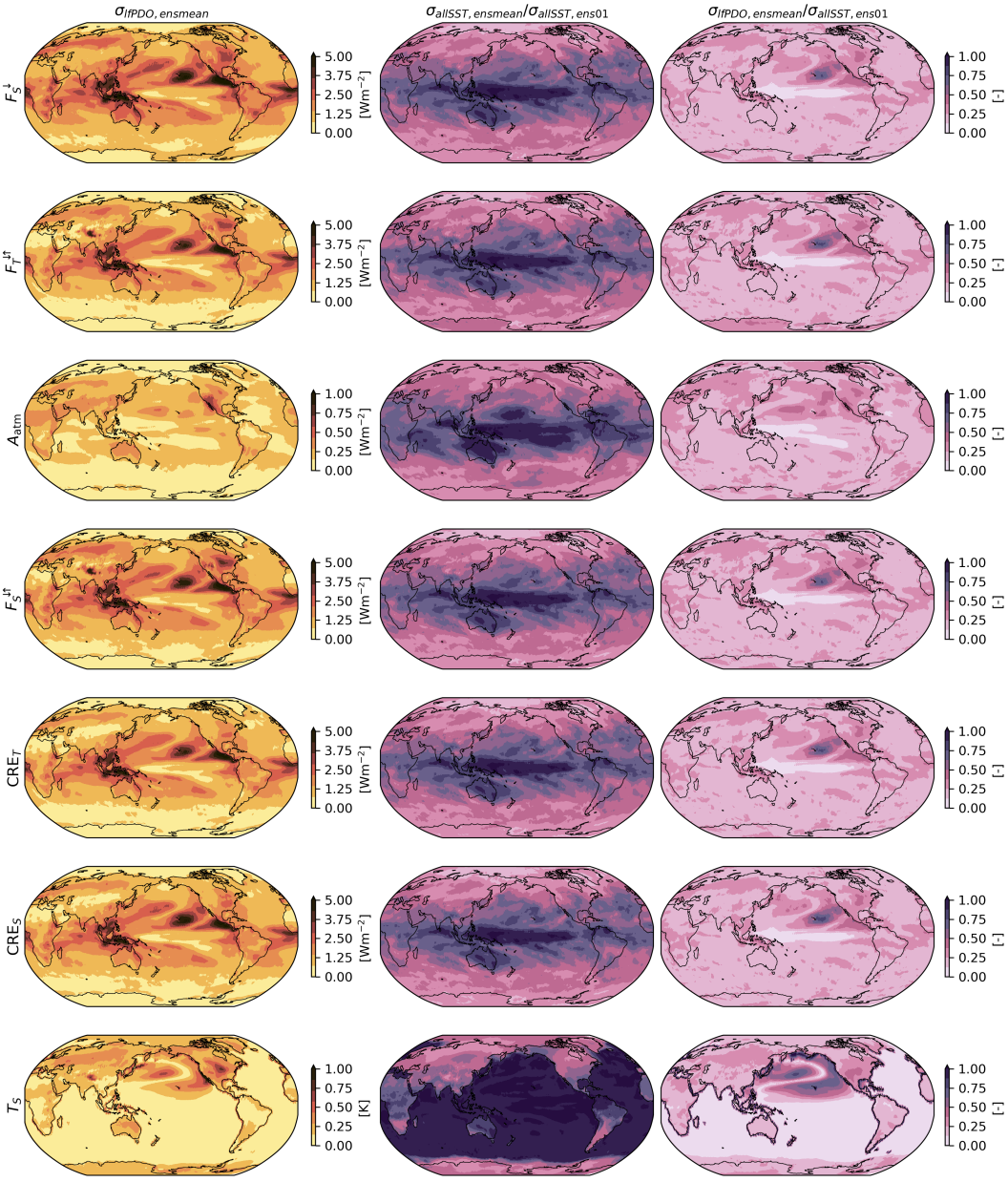

Figure 4. Standard deviation of the annual mean time series per grid box of the the 20-ensemble-member mean low frequency PDO experiment for different variables (first column), ratio between the standard deviation of the 20-ensemble-member mean in the all SST experiment and the standard deviation for the control run (second column) and ratio between the standard deviation of the 20-ensemble-member mean in the low-frequency PDO experiment and the control run (third column). The control run is one ensemble member of the all SST experiment.

need to separate atmosphere-only variability from SST-related atmosphere-ocean variability. We do so by running 20 ensemble members with SSTs directly taken from the coupled run ("allSST"): one ensemble member of this experiment (our control run) should possess both atmosphere and coupled variability. The atmosphere-only variability should be averaged out in the ensemble mean time series (average time series across ensemble

members for each grid box) and the only remaining variability in the 95-year ensemble mean should be related to the prescribed time-varying SSTs, as they are the only time-evolving boundary condition in our "allSST" experimental setup.

Taking this idea further, annual mean time series averaged over the 20 ensemble members of the "lfPDO" experiment should retain only variability associated with the low frequency PDO variability. The standard deviation of the latter (computed upon the 95-year ensemble mean time series per grid box) is shown on Figure 4, first column. We also show results for the surface temperature T_S (last row on Figure 4) because they best illustrate the direct effect of the experimental setup. Testing for a different number of ensemble members, we find the resulting reduction of variability converges for around 10 ensemble members.

To gain an impression of the relative importance of SST variability in general and PDO variability in particular, we compute the differences relative to the control run of the standard deviations of the time series per grid box as: $\sigma_{\mathrm{allSST,ensmean}}/\sigma_{\mathrm{allSST,ens01}}$, where $\sigma_{\mathrm{allSST,ensmean}}$ is the per grid box standard deviation of the ensemble mean time series (atmosphere-only variability is averaged out), and $\sigma_{\mathrm{allSST,ens01}}$ is the per grid box standard deviation of one of the ensemble members (our control run; includes atmospheric variability; results are not sensitive to the choice of specific ensemble member). The ratio is shown on Figure 4, second column. We see that SST-related variability is responsible for almost all of total (atmosphere and ocean) variability in the tropical regions. The standard deviation for the ensemble mean is reduced in roughly half for the shortwave flux variables for continental regions like North America and Europe (on a grid box level). Looking into spatially averaged (aggregated) time series instead of individual grid boxes (i.e. taking the spatially averaged time series and computing its standard deviation instead of averaging the standard deviations of the time series per grid box), the resulting ratio $\sigma_{\mathrm{allSST,ensmean}}/\sigma_{\mathrm{allSST,ens01}}$ is 10-30% more (not shown), i.e. SSTs explain a larger fraction of variability for spatially averaged time series across regions than for individual grid boxes. This is not surprising because the influence of the SSTs over land usually occurs thorough the large-scale circulation, the effect of which is reduced at the grid box level from small-scale noise and this small-scale noise is already averaged out in the aggregated time series, yielding a smaller reduction in variability. For the aggregated time series in our regions of interest, we find that the ratio is 0.78 for $F_S^{\downarrow}$ and 0.69 for $F_T^{\downarrow\uparrow}$ for North America, 0.53 for $F_S^{\downarrow}$ and 0.54 for $F_T^{\downarrow\uparrow}$ for Europe and 0.74 for both $F_S^{\downarrow}$ and $F_T^{\downarrow\uparrow}$ for India and Indochinese peninsula. The fraction of variability of CRE that can be related to the time evolving SSTs is 0.62 of the variability in the Northern Hemisphere (0.57 for North America, 0.45 for Europe and 0.67 for India and Indochinese peninsula).

The second step is to estimate how much of the total variability is related to the low-frequency PDO pattern. We do so by computing the ratio between the 20-ensemble-member mean in the "lfPDO" experiment and the control run: $\sigma_{\mathrm{lfpdo,ensmean}}/\sigma_{\mathrm{allSST,ens01}}$. The result (third column on Figure 4) is that the low frequency component of the PDO in our experimental setup is related to almost none of the variability in the tropics for the variables we investigate, it is also no or little related to the SST-related variability in Australia and South America. For the Northern Hemisphere aggregated time series, the PDO is related to a fraction of 0.37-0.44 (depending on the variable) of SST-related variability. For the shortwave radiative fluxes $\sigma_{\mathrm{lfpdo,ensmean}}/\sigma_{\mathrm{allSST,ens01}}$ this is 0.24-0.25 (depending on the variable) on average for individual grid boxes in the Northern Hemisphere. For spatially aggregated time series in the Northern Hemisphere, the fraction of total variability attributable to PDO is 0.33-0.35, for North America – 0.39-0.42, for Europe – 0.27-0.31, for India and Indochinese peninsula – 0.22-0.27. The fractions of variability presented in this section are indicative for the variability of annual mean time series and become larger for longer time scales, at which higher frequency atmospheric noise plays a smaller role (not shown).

3.3 Quantification of shortwave radiative flux anomalies associated with PDO phases

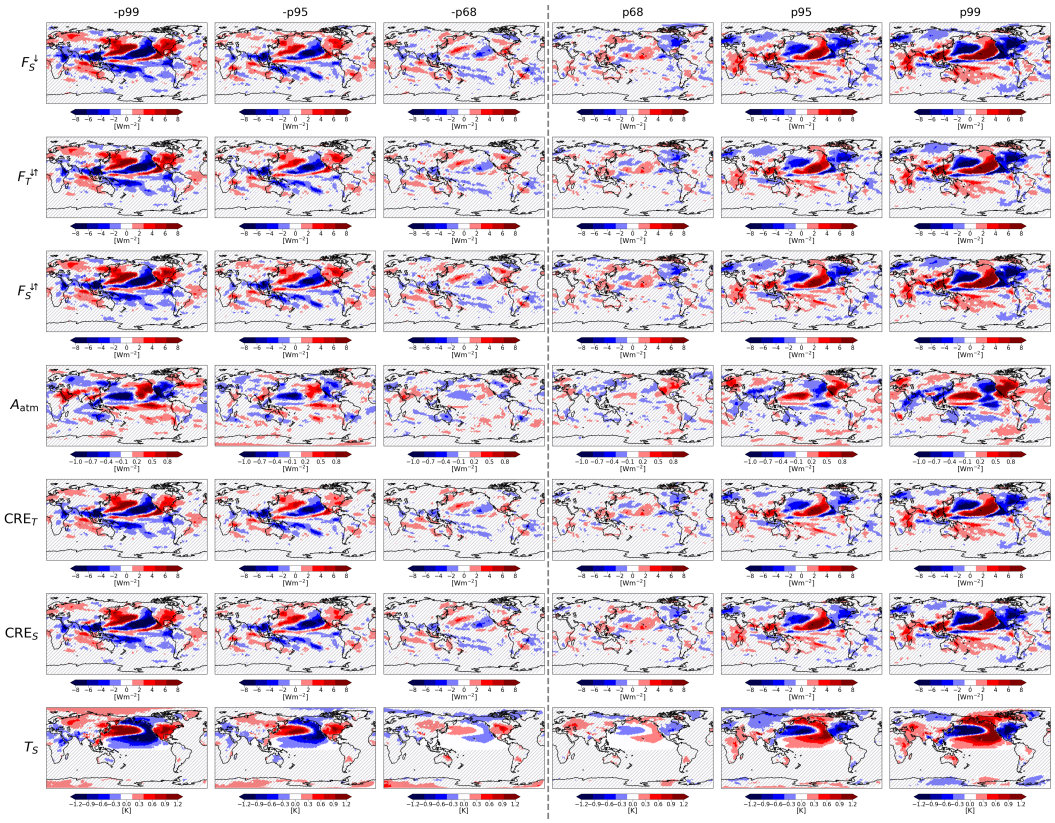

Figure 5. All-sky shortwave flux, cloud radiative effect and surface temperature anomalies computed for each "perpetual PDO" experiment ($\widetilde{PC}_1(t) \in [-2.58(-\text{p99}), -1.64(-\text{p95}), -0.44(-\text{p68}), 0.44(\text{p68}), 1.64(\text{p95}), 2.58(\text{p99})]$) relative to the control run ($\widetilde{PC}_1(t) = 0$). Hatched regions represent areas where the Student-t test is passed at the 0.05 significance level, i.e. the null hypothesis of equal population means of the two samples (time series in experiment and control in individual grid boxes) cannot be rejected.

We remove the temporal element of the PDO evolution and use the "perpetual" PDO set of simulations to quantify the increase in each of the radiative fluxes as a function of the PDO index value which is embroidered in the climatological SST field as anomalies in space (exact SST anomalies are shown on Figure A3). Each simulation is conducted with a constant in time PDO index value; the index values are chosen as different percentile of the distribution of all PDO index values obtained from the 500-year coupled simulation. By computing the difference between the mean time series of each experiment and the control run (neutral PDO), we obtain radiative flux anomalies per grid box which correspond to the different simulations (PDO indices). The spatial distribution of the radiative flux and surface temperature anomalies are shown on Figure 5. Comparing the spatial patterns to the trends distribution obtained from CMIP6 (Figure 2) for $F_S^{\downarrow}$, $F_T^{\downarrow\uparrow}$ and $F_S^{\downarrow\uparrow}$, we observe similarities in the Northern Hemisphere, including the North Pacific region, North America, Europe and Southern Asia. A prominent difference observed in the Southern hemisphere is Australia. In the fully-coupled CMIP6 simulations, where the PDO occurs in combination with other modes of ocean variability, Australia evolves in phase with South Asia. By contrast, in our simulations where the

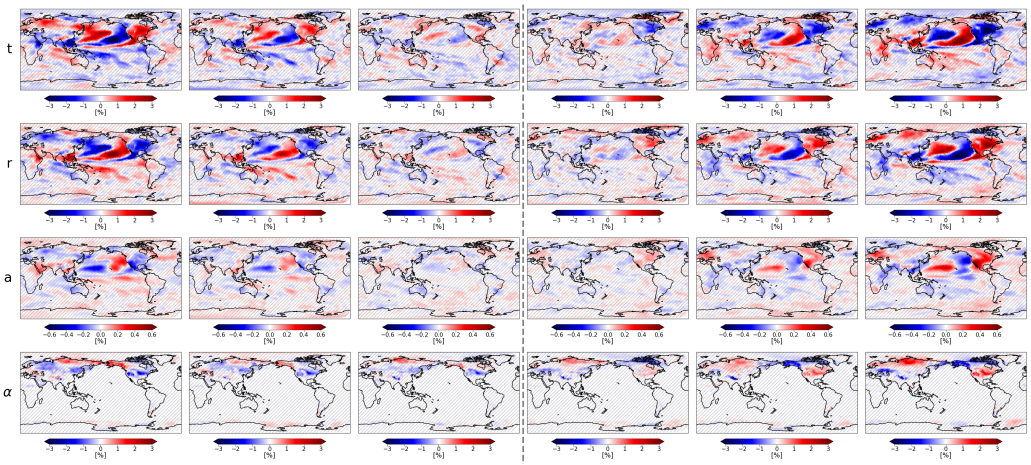

Figure 6. Same as Figure 5 but for anomalies in atmospheric transmittance, reflection, absorption and surface albedo.

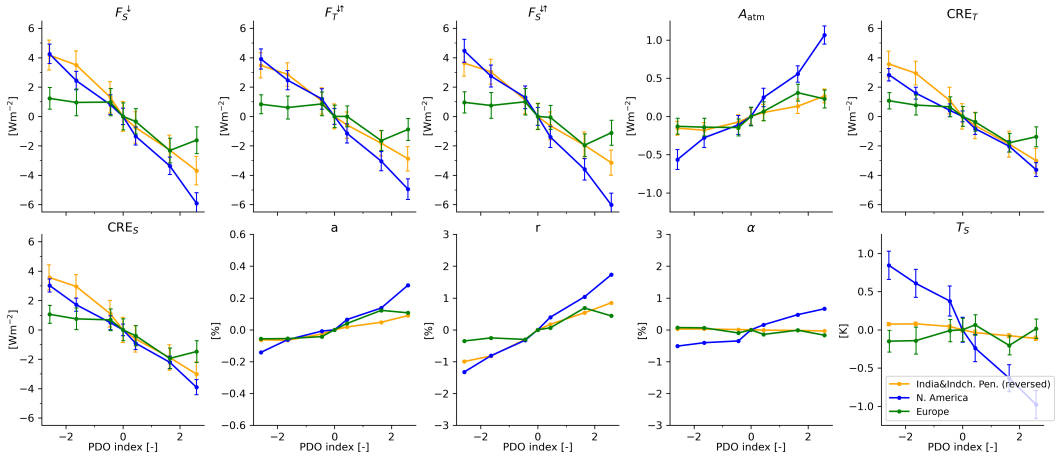

Figure 7. Scatter plots for different variables as a function of the PDO index value for regions denoted on Figure 2. The regional means for India and Indochinese peninsula are multiplied by −1. Uncertainty ranges show the 95% confidence interval determined via t-statistics. Values on y-axis depend on the exact choice of region boundaries, which is arbitrary.

PDO exists in isolation, this connection between Australia an South Asia is broken. The differences between our ICON-A simulations and CMIP6 will be further addressed in the discussion.

Comparing the simulations that differ in the strength and sign of the PDO SST anomaly (the different columns on Figure 5), we observe prominent and statistically significant differences in the simulations that correspond to higher percentiles (95, 99). In the p68, -p68 experiments, where the spatial SST anomaly is not as strong, the patterns of the radiative flux response cover smaller areas that appear scattered, but the resulting anomaly is of the same sign as in the simulations with stronger anomalies. We assess the statistical significance per grid box by performing Student t-test (Student, 1908) between the time series in the control run and the one in the corresponding experiments. Our null hypothesis that the two samples come from the same population is rejected in 23-29% (depending on the radiative flux variable) of the boxes in the Northern Hemi-

sphere for the p95 simulation and in 40-42% for the p99 simulation. These include most of the North Pacific Ocean, North America, South India, the Indochinese Peninsula and East Africa, more pronounced in the Ethiopian Highlands. The null hypothesis cannot be rejected at the 0.05 level for most of Europe (depending on the variable and experiment), indicating that the atmosphere-only variability can easily mask the PDO signal in a statistical test.

Based on the anomalies that correspond to -p95 and p95 (second and fifth columns on Figure 5), the surface and TOA radiative flux anomalies reach up to ± 6 Wm^{-2} for parts of North America, ∓ 3 Wm^{-2} for India and ± 2 Wm^{-2} for parts of Europe. These numbers represent per grid box anomalies associated with the PDO range of $[-1.64; 1.64]$ in the 95-year mean where atmospheric noise is averaged out.

To draw a more general picture and exploit the connections and similarities between the radiative fluxes, we decompose the observed changes to changes in the optical properties of the atmospheric column (transmittance, reflection and absorption) and changes in surface reflection (albedo) in relation to the PDO anomaly (our different simulations). To do so, we closely follow the decomposition described in Stephens et al. (2015) and Loeb et al. (2019), who use the upwelling and downwelling shortwave fluxes at TOA and at the surface: $F_T^{\downarrow} = S$ (downwelling shortwave at TOA), $F_T^{\uparrow}$, $F_S^{\downarrow}$, $F_S^{\uparrow}$. Exactly following Stephens et al. (2015), where further details may be found, we define the effective surface albedo α, the system transmittance T and the system reflectance R as:

$$\alpha = \frac{F_S^{\uparrow}}{F_S^{\downarrow}}, \tag{1}$$

$$R = \frac{F_T^{\uparrow}}{S} = r + \frac{t\alpha t}{1 - r\alpha}, \tag{2}$$

$$T = \frac{F_S^{\downarrow}}{S} = \frac{t}{1 - r\alpha}, \tag{3}$$

where t and r are the atmospheric transmissivity and reflection for a single beam, given the assumption that the atmosphere reflects and transmits equally in both upward and downward directions. The system reflectance R includes the reflected energy from the atmosphere rS plus the multiple scattering between the surface and atmosphere, it corresponds to Earth's planetary albedo (Stephens et al., 2015).

We can compute t and r from the T and R (and the radiative fluxes respectively) by:

$$t = T\frac{1 - \alpha R}{1 - \alpha^2 T^2} \tag{4}$$

$$r = R - t\alpha T \tag{5}$$

To better carve the energy partitioning, we express the atmospheric transmissivity t as:

$$t = 1 - a - r, \tag{6}$$

where $a = 1 - r - t$ is the fraction of the beam that is absorbed by the atmosphere. This gives a more clear separation on whether the excess energy that does not reach the surface goes into heating the atmosphere.

The spatial patterns of t, r, a and α are shown on Figure 6. It is evident that r closely resembles the patterns of changes in CRE (Figure 5), cloud cover, cloud liquid water and cloud ice content (not shown). a is similar to A_{atm}, as is to be expected, but their pattern does not closely follow the column integrated water vapour content (not shown), as clouds are also essential for atmospheric absorption (see section 3.1). The surface albedo α has its own unique pattern, which is enhanced when looking only at winter months (not shown), indicating that the changes are associated mainly with changes in snow cover.

There is an increase in α in North America during a positive PDO, in line with increased r in the region. Over Eurasia, the change in α is not symmetric for the positive and negative PDO phases: the increase in during a positive PDO seems to extend South to around 55°N, while during a negative phase, there is an increase in North Siberia (South to 60°N), and a decrease further South.

To draw whether the response of the large-scale radiative fluxes to the SST anomaly related to the PDO is linear or not, we take the anomalies of the spatially averaged time series in the regions discussed in the previous sections – North America, Europe and India and Indochinese peninsula and plot the mean anomalies for each simulations as a function of the "perpetual" PDO index driving the simulation. The anomalies are computed by aggregating the time series in the region, taking the time-mean across the last 95-years of the experiment run and subtracting the control run aggregated temporal mean. Resulting dependencies are shown on Figure 7 with the anomaly for India and Indochinese peninsula given with a negative sign to match the direction of the other curves. In the range of PDO indices we work in, the response of the radiative fluxes is mostly linear, even though there is asymmetry around zero for some regions and variables. For the aggregated time series in North America and India and Indochinese peninsula, the anomaly is about ± 4 Wm^{-2} for PDO index values of -2.58, 2.58 (-p99, p99 in the ICON-ESM-LR piControl distribution) and about about ± 1 Wm^{-2} for Europe. These values depend on the exact choice of the regions, which is only done for illustrative purposes and is arbitrary.

Results for Europe are indistinguishable from the control run, given the 95% confidence interval of the uncertainty of the mean, which is also evident from the statistical tests performed per grid box (Figure 5). However, the confidence intervals do not overlap for the highest and lowest PDO values, showing a distinct and statistically significant difference between the positive and negative values. The increase of both a and r from negative to positive PDO values, shows that they both contribute to the reduction $F_S^{\downarrow\uparrow}$ with the contribution of r being much larger. This is also evident when comparing the net radiative anomalies at the surface and TOA with $F_T^{\downarrow\uparrow}$ being always slightly smaller than $F_S^{\downarrow\uparrow}$, implying that the increased atmospheric absorption slightly offsets the reduction in $F_S^{\downarrow\uparrow}$ for a positive PDO phase. Unlike the radiative fluxes, the surface temperature, T_S, dependence is different in North America and Europe – the anomaly is negative in North America and small but positive in Europe, which is also evident in the patterns on Figure 5.

Lastly, we assess the relative contributions of t, a and α to changes in $F_S^{\downarrow}$ for the different PDO anomalies (simulations). We do so by expressing $F_S^{\downarrow}$ as:

$$F_S^{\downarrow} = \frac{1-r-a}{1-r\alpha} S \tag{7}$$

Since S in our case does not have any inter-annual variability and by also omitting covariance terms between δr, δa and $\delta\alpha$, we can approximate the change in $F_S^{\downarrow}$ as:

$$\begin{aligned}
\frac{\delta F_S^{\downarrow}}{S} &\approx \frac{-\delta a - \delta r}{1-r\alpha} - \frac{(1-r-a)(-r\delta\alpha - \alpha\delta r)}{(1-r\alpha)^2} \\
&= \delta r\Big(- \frac{1}{1-r\alpha} - \frac{-\alpha(1-r-a)}{(1-r\alpha)^2}\Big) + \delta a\Big(\frac{-1}{1-r\alpha}\Big) \\
&\quad + \delta\alpha\Big(\frac{(1-r-a)(-r)}{(1-r\alpha)^2}\Big) \\
&= k_1\delta r + k_2\delta a + k_3\delta\alpha.
\end{aligned} \tag{8}$$

The linear equation above allows us to attribute the changes in downwelling solar radiation $\delta F_S^{\downarrow}$ to changes in the atmospheric and surface properties: δr, δa and $\delta\alpha$. A similar expression can also be obtained for the net fluxes at the surface and TOA but for this we limit ourselves only to downwelling surface radiation.

Taking the relative contributions as $\delta aS/\delta F_S^{\downarrow}$, $\delta rS/\delta F_S^{\downarrow}$ and $\delta \alpha S/\delta F_S^{\downarrow}$, we find that for the individual regions they are approximately constant for the different PDO index values (i.e. relative contributions of the different terms do not change with the PDO value), especially the higher ones, where $\delta F_S^{\downarrow}$ is more distinct. The first thing we highlight is that the relative contributions depend on the region. For the ocean regions, where α is essentially constant, we note the following: in the Tropical extension of the PDO, almost all of the change in $F_S^{\downarrow}$ comes from changes in the reflectivity of the atmosphere δr; the same is true for the West part of the PDO region (cold region during a positive PDO phase) with only 2-3% of the changes in $F_S^{\downarrow}$ being attributable to δa; in the East part of the PDO (warm region during a positive phase), 86% of the changes in $F_S^{\downarrow}$ are attributable to δr and around 14% to δa. Over India and Indochinese peninsula, 91% of the changes are attributable to δr and around 9% to δa. In the North American region, 93% of the changes can be attributed to δr, 13% – to δa, and 6% are offset by $\delta \alpha$, which dampens the reduction in $F_S^{\downarrow}$ by increased snow cover during the positive PDO phase and the other way around for the negative phase. For Europe (excluding Scandinavia), the increase in r and a, and a reduction in α, all contribute to a reduction in $F_S^{\downarrow}$ by 80%, 17% and 3% respectively. All percentages given are average contributions of the terms for the -p99, -p95, p95 and p99 simulations. The residual contributions of the covariance terms are less than 0.1% for all regions and experiments investigated.

4 Discussion

The discussion section is structured as follows: in the first part we compare results from our "perpetual" PDO ICON-A simulations to the coupled ICON-ESM-LR and CMIP6 multi-model median to carve out differences that are due to coupling and differences between ICON and the median across CMIP6 models. In the second part, we compare the PDO index amplitudes within ICON and observations, namely ERSST V5 (Huang et al., 2017).

Comparing the patterns between Figures 2 (CMIP6) and 5 (ICON-A), we observe differences in the shortwave radiative fluxes in the Southern Hemisphere, Australia, South America, the Arab peninsula and Sahara, Atlantic ocean and the Arctic. The radiative flux patterns for Australia, South Pacific, and South America are evident in both CMIP6 multi-model median (Figure 2) and ICON-ESM-LR (Figure B1), implying that they result from the coupling or a large-scale process related to the PDO that is not included in our experimental setup rather than differences between the ICON model and CMIP6. This suggests that the mechanisms responsible for Australian and South American radiative flux anomalies do not depend only on the PDO as a horseshoe phenomenon in the North Pacific, but on its basin-wide manifestation – IPO, which does not exist in that form in our "PDO only" simulations. Furthermore, the radiative fluxes in the South Pacific appear to be affected in a similar (but weaker) way as in CMIP6, which in a coupled simulation would have an effect on the SSTs and the dynamics thereafter. This change in the shortwave radiative fluxes (including unforced dimming and brightening) might be one of the mechanisms through which Northern extratropics communicate with Southern hemisphere and PDO influences the SPDO and they combine into IPO.

The dimming above the Atlantic during PDO↑ that is evident in CMIP6 and ICON-ESM-LR (Figure B1) but not in our ICON-A (Figure 5) simulations implies that it either arises from the interaction between the atmosphere and ocean or there are other processes, independent from the North Pacific horseshoe pattern, that are related to the PDO. A mechanism that we propose is that the North Atlantic dimming in the coupled models might arise from the ocean transport (by surface currents like the Gulf stream) of cold waters from the East coast of North America into the ocean interior. The East coast is influenced by PDO-related dimming that is also evident in our atmosphere-only ICON-A simulations. This gives a hypothetical example of a communication mechanism between the North Pacific and North Atlantic oceans through surface shortwave fluxes.

The difference in the region of the Mediterranean Sea, Arab peninsula and Sahara: dimming in CMIP6 multi-model median and no-specific response or weak brightening in our ICON-A (Figure 5) simulations are also evident between the CMIP6 multi-model median (Figure 2) and ICON-ESM-LR (Figure B1), which implies that they are due to differences in the specific model response of ICON.

We also highlight that the correlation coefficients between ICON-ESM-LR and the shortwave fluxes are higher as compared to the majority of CMIP6 models, but such high correlation coefficients are also evident in model families such as CESM2, CMCC, GFDL and MIROC (Table 1). This stronger relationship is also evident in the stronger trend magnitudes in ICON-ESM-LR (Figure B1) as compared to CMIP6 multi-model median (Figure 2). It is also related to the large inter-model spread in the trend magnitudes estimated in section 3.1. Whether the differences among models are due to a weaker SST anomaly or a different atmospheric response requires further investigation.

We next compare the PDO that we derived from ICON-ESM-LR to the PDO time series computed with the same method upon the ERSST-v5 reconstructed SST data (Huang et al., 2017) that covers the period 1920-2015 on a 2°grid with a monthly resolution. We decrease the imprint of global warming on the observational SST field by subtracting the global annual mean SST anomaly from each grid box. Extracting the first eigenvector (that corresponds to the PDO horseshoe) from the deseasonalized monthly anomalies in the observations, yields the historical PDO time series. The variance fraction explained by this principal component is 17%, in comparison for ICON-ESM-LR, the variance fraction is 25% (based on the ratio between the first eigenvalue divided by the sum of all eigenvalues). To account for differences in the variance fraction, the principal component time series are usually normalized by their eigenvalues, which relates the magnitude of the spatial pattern (EOF) and the temporal variability (PC). We then compare the 95^{th} percentiles of the resulting distributions of PDO index values, that are 1.64 for ICON-ESM-LR and 1.58 for ERSST-v5, yielding a slightly stronger PDO amplitudes in ICON-ESM-LR as compared to ERSST-v5. The differences in variance fraction also imply that the observational SST field contains much more "noise" on top of the idealized PDO evolution that we analyse in this study. The pattern correlation for PDO between the ICON-ESM-LR and ERSST-v5 is 0.85 (computed on the ICON grid), typical for CMIP model ranges of 0.8-0.9 (Newman et al., 2016).

One might pose the question on why we use SSTs from the coupled piControl run instead of directly taking them from observations. The reasons for this are the following: (1) the piControl simulation is not contaminated by global warming and climate change; (2) we can build better statistics and derive a cleaner eigenvector from 500 years of data as compared to the shorter observational period; (3) the atmospheric dynamics within the model is aligned with the SSTs, which might be of relevance because SST patterns are a combination of atmospheric and oceanic processes and having a numerical mismatch between the atmosphere and SSTs might compromise a study that focuses solely on internal variability. Given the comparison to observed SSTs above, we do not have indications of significant biases in the PDO pattern selected for our experiments.

5 Summary

The present study targets the role of one specific mode of ocean variability – the PDO, in the variability of the shortwave flux components within Earth's energy balance: $F_S^{\downarrow}$, $F_T^{\downarrow\uparrow}$, $F_S^{\downarrow\uparrow}$, A_{atm}, CRE_S, CRE_T. First, we look at them through the lens of the PDO in coupled simulations, i.e. the PDO as it is diagnosed via the PDO index in CMIP6 piControl simulations, where the it is naturally co-occurring with other modes of variability, notably ENSO and the SPDO. Seen through this PDO lens, the all-sky components of $F_S^{\downarrow}$, $F_T^{\downarrow\uparrow}$, $F_S^{\downarrow\uparrow}$, CRE_S, CRE_T show remarkably similar patterns associated with the PDO, highlighting the redistribution of clouds in sync with the PDO in the coupled system.

On the other hand, changes of all-sky A_{atm} and the clear-sky components in relationship to the PDO show different patterns that reflect the redistribution of shortwave absorbers in the atmosphere (mainly water vapour) and changes in effective surface albedo in response to PDO.

Adjusting the PDO lens to focus, by experiment design, exclusively on the North Pacific horseshoe and its year-to-year variability, we ask the question what is the fraction of total year-to-year variability that can be related to the PDO. To do so, we run ensemble amtosphere-only simulations with ICON-A (each with length 100 years) that allow us to average out atmosphere-only variability for an all SST ("allSST") case and a low frequency PDO case ("lfPDO"). The "allSST" experiment contains the SSTs directly taken from the coupled piControl run of ICON-ESM-LR, while the "lfPDO" experiment contains only the low-frequency component of the PDO time series projected on the SST field. We show that SST-related variability (including ENSO) is related to almost all variability of shortwave fluxes in the tropics and about half of the variability in the extratropics. The PDO alone (constrained to the North Pacific) is related to almost none of the variability in the tropics and around 20-40% of variability of the shortwave fluxes over the Northern Hemispheric continents. We also show that over land, SST-related variability is more evident in spatially averaged (aggregated) time series as compared to individual grid boxes. This is because the SSTs impact on large-scale dynamics is prone to be blurred by small-scale noise.

Keeping the idealized spatial form of the PDO lens but now idealizing also the temporal manifestation, we carry out a set of "perpetual" PDO simulations, each corresponding to a different PDO anomaly in space. When comparing the geographical patterns of shortwave flux anomalies we obtain this way to geographical patterns of trends within the CMIP6 data set, we find overall agreement in the Northern Hemisphere. We show that the mean anomalies on a grid box level for North America reach up to ± 6 Wm^{-2}; for India and Indochinese peninsula – up to ∓ 3 Wm^{-2}; and for Europe – up to ± 2 Wm^{-2}. Numbers represent anomalies associated with the PDO range of $[-1.64; 1.64]$ (-p95 and p95) taken from the temporal mean of each 100-year simulation, where atmospheric variability is averaged out.

Focusing on changes in $F_S^{\downarrow}$, induced by the PDO, we find that the relative contributions of changes in fractional atmospheric reflection r, absorption a, and effective surface albedo α depend on the region. r (primarily related to clouds) has the largest contribution in all regions with α (primarily related to snow cover) slightly offsetting the effect for North America and a (related to both water vapour and clouds) playing a larger role for PDO-related $F_S^{\downarrow}$ anomalies in Europe and a smaller role for India and Indochinese peninsula. Magnitudes in $F_T^{\downarrow\uparrow}$ are in general less than those in $F_S^{\downarrow\uparrow}$, which is explained by the increase of both r and a in those regions – increased atmospheric absorption slightly offsets the decrease in absorption at the surface.

The combined view through these different PDO lenses, ranging from a "realistic" PDO embedded in its natural context of other modes of variability in CMIP6 to a highly idealized, eternally phase locked PDO within our ICON-A simulations, inspires some hypotheses and speculations. By assessing the similarities and differences in these patterns, we mark regions that show a different response in coupled and atmosphere-only simulations. The radiative flux anomalies in the South Pacific ocean evident in the idealized atmosphere-only simulations suggest that the North Pacific PDO impacts the South Pacific through changes in r (clouds). The resulting change in $F_S^{\downarrow}$ (dimming and brightening) might be one of the mechanisms through which Northern extratropics communicate with Southern extratropics and in the SST field: PDO and SPDO combine into IPO. We also note that a similar mechanism might be present for the North Atlantic – during a positive PDO phase, dimming over the East coast of North America (evident in the atmosphere-only simulations) can cool the surrounding waters, which in a coupled run are transported via ocean currents, resulting in dimming throughout the path

of the Gulf stream in the North Atlantic (as seen in the coupled simulations). Thus, unforced decadal changes in the shortwave radiative fluxes, like dimming and brightening, appear to participate in sustaining (in the North Pacific) and maybe forcing (in the South Pacific and North Atlantic oceans) decadal scale SST trends, which highlights their importance for atmosphere-ocean modes in the coupled system.

Appendix A Appendix: Detailed experiment design

Here we give a detailed description of the modification we perform on the SST field used in the ICON-A simulations. We start by obtaining the monthly mean SSTs from the coupled ICON-ESM-LR piControl run that is 500 years of length. We take the temperature at the lower boundary of the atmosphere (surface temperature, ts) that is already on the grid of the atmospheric model (R2B4, grid id 0013). We deseasonalize the data by subtracting the climatological mean for each month. We extract the surface temperature of non-land grid boxes using the ICON grid description and we arrange the SST field in a 2D matrix of time and space: $SST(t, x_{\text{all}})$, where $t \in [0; 6000)$ represents 500 years of monthly data and $x_{all} \in [0; 13132)$ represents all non-land grid boxes on the ICON grid. We further restrict the region of interest to the North Pacific bounding box: 20-70°N and 110-260°E. The resulting field $SST(t, x_{\text{reg}})$ with $x_{\text{reg}} \in [0, 1522)$, we decompose into a set of principal components $PC_i(t)$ and empirical orthogonal functions $EOF_i(x_{reg})$, weighted to the area of each grid box (singular value decomposition):

$$SST(t, x_{\text{reg}}) = \sum_{i=1}^{i_{\max}} PC_i(t) \otimes EOF_i(x_{\text{reg}}), \tag{A1}$$

where $i_{\max} = 1522$ corresponds to the number of grid boxes in x_{reg}. By definition, $PC_1(t)$ and $EOF_1(x_{reg})$ correspond to the PDO time series and spatial pattern. The spatial pattern expressed as correlations is shown on Figure A1-a.

The main mathematical challenge is to have a smooth transition of the field outside the geographical box in which the EOF decomposition is performed (If the decomposition is performed on a larger box, the resulting EOF_1 bears the strong tropical fingerprint of ENSO.) In order to expand $EOF_1(x_{\text{reg}})$ into the larger domain, we use a method referred to as Empirical Orthogonal Function Teleconnections, or EOF Regression or Teleconnection Patterns (van den Dool et al., 2000). The method relies on expanding each $EOF_i(x_{\text{reg}})$ by computing the slope of linear regression between $SST(t, x_j)$ and $PC_i(t)$ for each grid box (x_j). The outer product of the obtained map of regression coefficients $s_i(x_{\text{all}})$ and $PC_i(t)$ gives us the reconstructed field for the i-th principal component:

$$\widetilde{SST}(t, x_{\text{all}}) = PC_i(t) \otimes s_i(x_{\text{all}}). \tag{A2}$$

In general, if we were to obtain a realistic field that represents a larger fraction of variability, we would have to obtain a linear regression coefficient map for each principal component and sum over all of them. Since our goal is to have a field containing variability only related to the first one, we simply:

$$\widetilde{SST}(t, x_{\text{all}}) = PC_1(t) \otimes s_1(x_{\text{all}}). \tag{A3}$$

This process uses the linear relationship between $SST(t, x)$ and $PC_1(t)$, contained in $s_1(x)$ to reconstruct the field in the larger domain (x_{all}). By design, singular value decomposition represents the field as a linear combination of modes (eigenvectors), and their corresponding PCs. Mathematically, the reconstruction yields identical results in the region of x_{reg} but extended to a larger domain. Since the decomposition is not done in the larger domain, we do not have the proper eigenvectors to reconstruct back the whole field but this is not our intention as we are only interested in the primary principal component and its extended eigenvector.

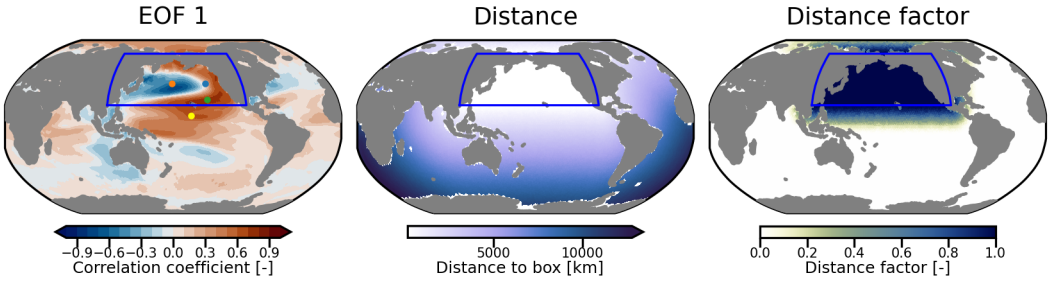

Figure A1. Left plot shows first EOF expressed as the correlation with the monthly SST time series for each grid box, blue box shows the region in which the EOF decomposition is done (same as on Figure 1. Superimposed points align with those presented in Figure A2. Middle plot shows the distance of each grid box from the boarder of the PDO box (blue box). Right plot shows the corresponding distance factor, obtained via the sin^2 function. The distance factor equals 1 inside the box and 0 at distances exceeding 3000 km.

The idea of extending the spatial field from x_{reg} to x_{all} was for a smooth transition of the projected field outside the boundaries of the North Pacific box. We do this by first computing the distance between the center of each grid box and the closest grid box within the North Pacific box: d. The resulting Distance map is shown on Figure A1-b. We decide on a maximum distance away from the region in which we modify the field of $d_{max} = 3000$ km. We construct a distance factor d_f that is:

$$d_f = \begin{cases} 1 & \text{if inside the N. Pacific box} \\ \sin\left(\frac{\pi}{2} \times \frac{d - d_{\max}}{d_{\max}}\right)^2 & \text{if } d < d_{\max} \\ 0 & \text{if } d >= d_{\max} \end{cases} \tag{A4}$$

The resulting d_f map is shown on Figure A1-c. When projecting an arbitrary $\widetilde{PC}_1(t)$ in the form of anomaly time series to obtain a SST field, we simply multiply the time series by d_f. Climatological values per grid box are added in the end to obtain a realistic field with seasonality.

We perform the following experiments, each 100 years of length:

1. "piSST": SST taken directly from the coupled CMIP6 run. They correspond to the first 100 years (4001-4101) in the ICON-ESM-LR piControl simulation.
2. "lfPDO": Project $\widetilde{PC}_1(t)$ that is obtained after low-pass filtering the original $PC_1(t)$ with a filter in the form of a sharp logarithmic function in frequency space: $F = (a_1/a_0)^{f_i/(N-1)}$ for frequencies f_i higher than $f_{min} = 0.00833$ cycles/month, which corresponds to 10 years in monthly values. The coefficients are $a_1 = 10^{-7}$ and $a_0 = 1$. $N = 6000$ is the length of the input data in the form of deseasonalized monthly anomalies. The resulting $\widetilde{PC}_1(t)$ time series and its power spectra are shown on Figure 1. Its projection as SST anomalies is shown on Figure A2.
3. "Perpetual PDO" simulations, each corresponding to a different percentile (p) of the distribution of the original $PC_1(t)$ monthly values and we project a constant in time $\widetilde{PC}_1$(t):
   (a) $\widetilde{PC}_1(t) = const = 2.58$ (p99)
   (b) $\widetilde{PC}_1(t) = const = 1.64$ (p95)
   (c) $\widetilde{PC}_1(t) = const = 0.44$ (p68)

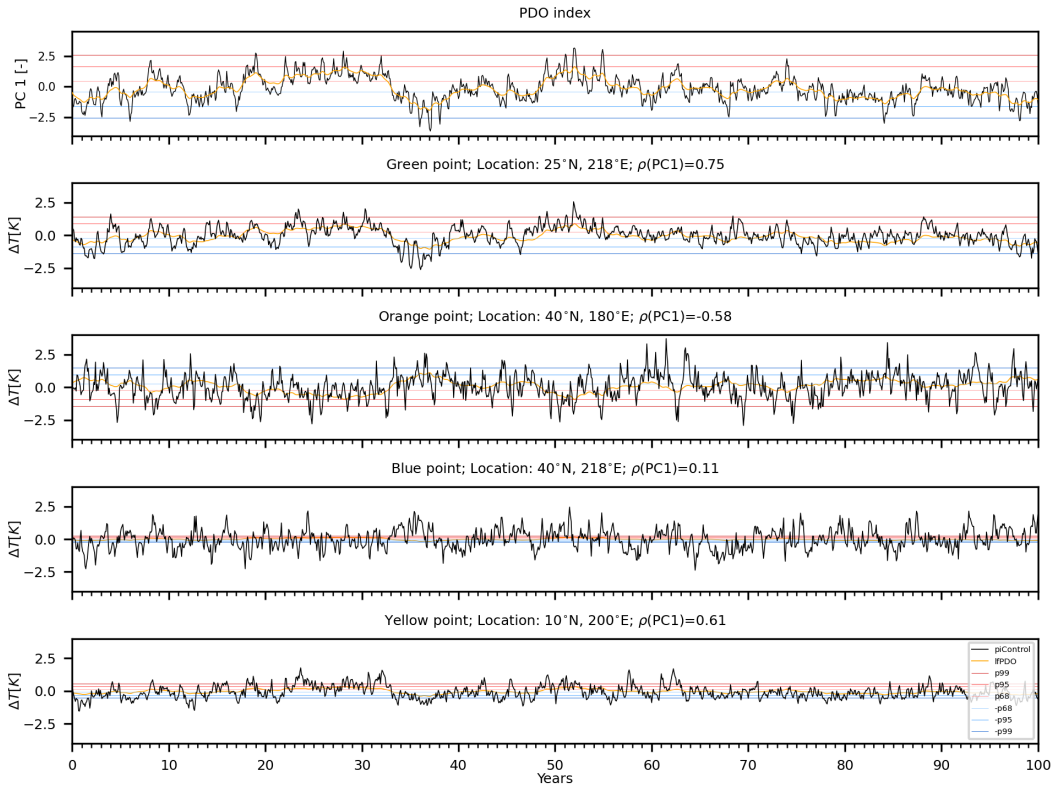

Figure A2. Time series of the first principal component and deseasonalized monthly SST anomalies at different locations, depicted on Figure A1 for 100 years. The green point as chosen with a strong positive correlation with PC1 (ρ(PC1)), the orange point – with a strong negative, the blue point – weak correlation. The yellow point is strongly correlated to PC1 but lies outside the analysis box and is affected by the distance factor. Black curve shows the original SST time series from the piControl run (also the control simulation), orange curve shows time series from SST field after projecting the low-pass filtered PC1. Gray lines depict the climatological simulation (all values are zero), blue lines depict locked negative phase PDO simulations and red lines – locked positive phase PDO simulations. Seasonality is not shown on the plots but included in the SST boundary conditions.

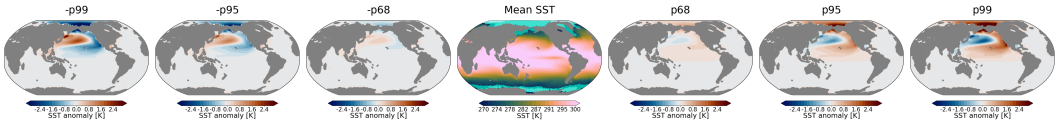

Figure A3. SST anomaly associated with different percentiles (p) of the monthly PDO index distribution that we uses for the corresponding experiments. Middle plot shows the mean SST field on top of which we add the anomalies and the three shades of turquoise represent the maximum, mean and minimum extent of sea ice within one year.

(d) $\widetilde{PC}_1(t) = const = 0$ (p50, control run)

(e) $\widetilde{PC}_1(t) = const = -0.44$ (-p68)

(f) $\widetilde{PC}_1(t) = const = -1.64$ (-p95)

(g) $\widetilde{PC}_1(t) = const = -2.58$ (-p99)

For a better illustration of how the SST field is being modified for each experiment, we include the anomaly time series (before adding the seasonality) for different grid boxes on Figure A2. The locations of the points are shown on Figure A1-a and we choose them as: the green point represents a location with a strong positive correlation with the $PC_1(t)$ time series; the orange point - strong negative correlation; the blue point is within the North Pacific box but is not correlated with the $PC_1(t)$ time series; and the yellow point is strongly correlated with the $PC_1(t)$ time series but lies outside the North Pacific box and is therefore again weakly affected by our modification (projected anomalies are smaller in magnitude as compared to the green and orange points). The spatial representation for each of the $\widetilde{PC}_1(t) = const$ projections is given on Figure A3, where we also show the mean SST field and the climatology of sea ice that is kept constant across simulations, i.e. does not exhibit any inter-annual variability.

Appendix B Appendix: Patterns for ICON-ESM-LR

The all-sky and clear-sky shortwave flux and cloud radiative effect trend patterns during 20-year periods with a strong phase transition of the PDO index for ICON-ESM-LR are shown to complement the patterns of the multi-model median of CMIP6 in Figures 2-3.

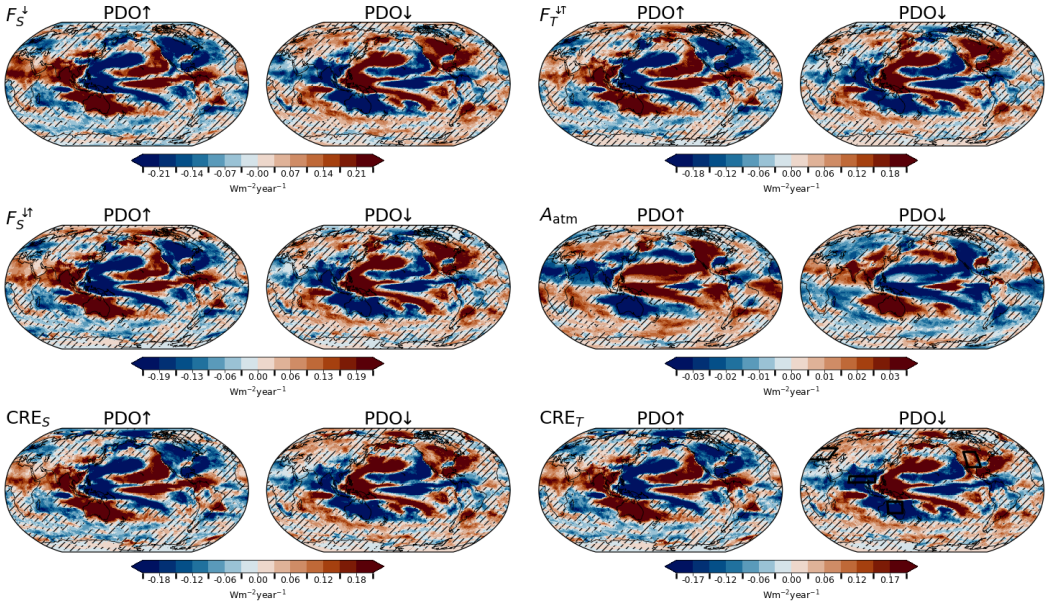

Figure B1. Same as Figure 2 but only for the piControl simulation of ICON-ESM-LR.

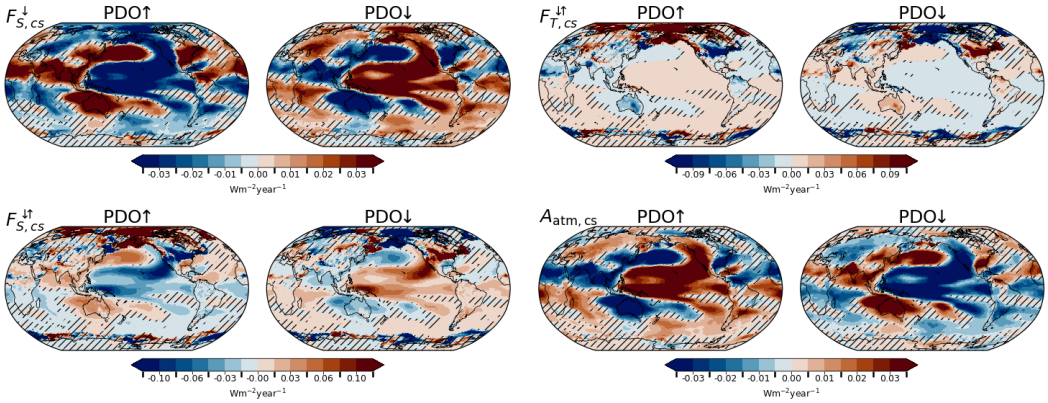

Figure B2. Same as Figure 3 but only for the piControl simulation of ICON-ESM-LR.

Open Research Section

Data from the Coupled Model Inter-comparison Project—Phase 6 were used in the manuscript (Eyring et al., 2016). Climate indices were computed using the Climate variability diagnostics package (CVDP) (Phillips et al., 2014). Observational sea surface temperatures are taken from the NOAA Extended Reconstructed SST V5 (ERSST) (Huang et al., 2017).

Acknowledgments

This work was funded by Swiss National Science Foundation Grant 200020_188601. The numerical simulations were realized through a grant from the Swiss National Supercomputing Centre (CSCS) under project ID s1144. We acknowledge the World Climate Research Programme, which, through its Working Group on Coupled Modelling, coordinated and promoted CMIP6. We thank the climate modeling groups for producing and making available their model output, the Earth System Grid Federation (ESGF) for archiving the data and providing access, and the multiple funding agencies who support CMIP6 and ESGF. The data analysis and visualization have been performed using exclusively free and open source software (including Linux, Python, and CDO): we would like to thank the community for building powerful tools from which everyone can benefit.

References

Allan, R. P., Liu, C., Loeb, N. G., Palmer, M. D., Roberts, M., Smith, D., & Vidale, P.-L. (2014, aug). Changes in global net radiative imbalance 1985-2012. *Geophysical Research Letters*, *41*(15), 5588–5597. Retrieved from https://doi.org/10.1002%2F2014gl060962 doi: 10.1002/2014gl060962

Augustine, J. A., & Capotondi, A. (2022, aug). Forcing for multidecadal surface solar radiation trends over northern hemisphere continents. *Journal of Geophysical Research: Atmospheres*, *127*(16). Retrieved from https://doi.org/10.1029%2F2021jd036342 doi: 10.1029/2021jd036342

Chen, X., & Wallace, J. M. (2015, dec). ENSO-like variability: 1900–2013∗. *Journal of Climate*, *28*(24), 9623 − −9641. *Re*
doi: 10.1175/jcli-d-15-0322.1

Chtirkova, B., Folini, D., Correa, L. F., & Wild, M. (2022, jun). Internal variability of all-sky and clear-sky surface solar radiation on decadal timescales. *Journal of Geophysical Research: Atmospheres*, *127*(12). Retrieved from https://doi.org/10.1029%2F2021jd036332 doi: 10.1029/2021jd036332

Chtirkova, B., Folini, D., Correa, L. F., & Wild, M. (2023, jun). Internal variability of the climate system mirrored in decadal-scale trends of surface solar radiation. *Journal of Geophysical Research: Atmospheres*, *128*(12). Retrieved from https://doi.org/10.1029%2F2023jd038573 doi: 10.1029/2023jd038573

Crueger, T., Giorgetta, M. A., Brokopf, R., Esch, M., Fiedler, S., Hohenegger, C., ... Stevens, B. (2018, jul). ICON-a, the atmosphere component of the ICON earth system model: II. model evaluation. *Journal of Advances in Modeling Earth Systems*, *10*(7), 1638–1662. Retrieved from https://doi.org/10.1029%2F2017ms001233 doi: 10.1029/2017ms001233

Donohoe, A., Armour, K. C., Pendergrass, A. G., & Battisti, D. S. (2014, nov). Shortwave and longwave radiative contributions to global warming under increasing CO_2. *Proceedings of the National Academy of Sciences*, *111*(47), 16700–16705. Retrieved from https://doi.org/10.1073%2Fpnas.1412190111 doi: 10.1073/pnas.1412190111

Eyring, V., Bony, S., Meehl, G. A., Senior, C. A., Stevens, B., Stouffer, R. J., & Taylor, K. E. (2016, may). Overview of the coupled model intercomparison project phase 6 (CMIP6) experimental design and organization. *Geoscientific Model Development*, *9*(5), 1937–1958. Retrieved from https://doi.org/10.5194%2Fgmd-9-1937-2016 doi: 10.5194/gmd-9-1937-2016

Folini, D., Dallafior, T. N., Hakuba, M. Z., & Wild, M. (2017, jan). Trends of surface solar radiation in unforced CMIP5 simulations. *Journal of Geophysical Research: Atmospheres*, *122*(1), 469–484. Retrieved from https://doi.org/10.1002%2F2016jd025869 doi: 10.1002/2016jd025869

Folland, C. K. (2002). Relative influences of the interdecadal pacific oscillation and ENSO on the south pacific convergence zone. *Geophysical Research Letters*, *29*(13). Retrieved from https://doi.org/10.1029%2F2001gl014201 doi: 10.1029/2001gl014201

Giorgetta, M. A., Brokopf, R., Crueger, T., Esch, M., Fiedler, S., Helmert, J., ... Stevens, B. (2018, jul). ICON-a, the atmosphere component of the ICON earth system model: I. model description. *Journal of Advances in Modeling Earth Systems*, *10*(7), 1613–1637. Retrieved from https://doi.org/10.1029%2F2017ms001242 doi: 10.1029/2017ms001242

Harris, C. R., Millman, K. J., van der Walt, S. J., Gommers, R., Virtanen, P., Cournapeau, D., ... Oliphant, T. E. (2020, September). Array programming with NumPy. *Nature*, *585*(7825), 357–362. Retrieved from https://doi.org/10.1038/s41586-020-2649-2 doi: 10.1038/s41586-020-2649-2

Henley, B. J., Gergis, J., Karoly, D. J., Power, S., Kennedy, J., & Folland, C. K. (2015, mar). A tripole index for the interdecadal pacific oscillation. *Climate Dynamics*, *45*(11-12), 3077–3090. Retrieved from https://doi.org/10.1007%2Fs00382-015-2525-1 doi: 10.1007/s00382-015-2525-1

Huang, B., Thorne, P. W., Banzon, V. F., Boyer, T., Chepurin, G., Lawrimore, J. H., ... Zhang, H.-M. (2017). *[dataset] noaa extended reconstructed sea surface temperature (ersst), version 5.* NOAA National Centers for Environmental Information. Retrieved from https://data.nodc.noaa.gov/cgi-bin/iso?id=gov.noaa.ncdc:C00927 doi: 10.7289/V5T72FNM

IPCC. (2021). *Climate change 2021: The physical science basis. contribution of working group i to the sixth assessment report of the intergovernmental panel on climate change* [Book]. Cambridge, United Kingdom and New York, NY, USA: Cambridge University Press. Retrieved from https://www.ipcc.ch/report/ar6/wg1/

Jungclaus, J. H., Lorenz, S. J., Schmidt, H., Brovkin, V., Brüggemann, N., Chegini, F., ... Claussen, M. (2022, apr). The ICON earth system model version 1.0. *Journal of Advances in Modeling Earth Systems*, *14*(4). Retrieved from https://doi.org/10.1029%2F2021ms002813 doi: 10.1029/2021ms002813

Liu, Z., Tang, Y., Jian, Z., Poulsen, C. J., Welker, J. M., & Bowen, G. J. (2017, mar). Pacific north american circulation pattern links external forcing and north american hydroclimatic change over the past millennium. *Proceedings of the National Academy of Sciences*, *114*(13), 3340–3345. Retrieved from https://doi.org/10.1073%2Fpnas.1618201114 doi: 10.1073/pnas.1618201114

Loeb, N. G., Johnson, G. C., Thorsen, T. J., Lyman, J. M., Rose, F. G., & Kato, S. (2021, July). Satellite and ocean data reveal marked increase in earth's heating rate. *Geophysical Research Letters*, *48*(13). Retrieved from https://doi.org/10.1029/2021gl093047 doi: 10.1029/2021gl093047

Loeb, N. G., Thorsen, T., Norris, J., Wang, H., & Su, W. (2018, July). Changes in earth's energy budget during and after the "pause" in global warming: An observational perspective. *Climate*, *6*(3), 62. Retrieved from https://doi.org/10.3390/cli6030062 doi: 10.3390/cli6030062

Loeb, N. G., Wang, H., Rose, F. G., Kato, S., Smith, W. L., & Sun-Mack, S. (2019, jul). Decomposing shortwave top-of-atmosphere and surface radiative flux variations in terms of surface and atmospheric contributions. *Journal of Climate*, *32*(16), 5003–5019. Retrieved from https://doi.org/10.1175%2Fjcli-d-18-0826.1 doi: 10.1175/jcli-d-18-0826.1

Mann, H. B., & Whitney, D. R. (1947, March). On a test of whether one of two random variables is stochastically larger than the other. *The Annals of Mathematical Statistics*, *18*(1), 50–60. Retrieved from https://doi.org/10.1214/aoms/1177730491 doi: 10.1214/aoms/1177730491

Mantua, N. J., & Hare, S. R. (2002).

Journal of Oceanography, *58*(1), 35–44. Retrieved from https://doi.org/10.1023%2Fa%3A1015820616384 doi: 10.1023/a:1015820616384

Meyssignac, B., Chenal, J., Loeb, N., Guillaume-Castel, R., & Ribes, A. (2023, jul). Time-variations of the climate feedback parameter are associated with the pacific decadal oscillation. *Communications Earth &amp Environment*, *4*(1). Retrieved from https://doi.org/10.1038%2Fs43247-023-00887-2 doi: 10.1038/s43247-023-00887-2

Newman, M., Alexander, M. A., Ault, T. R., Cobb, K. M., Deser, C., Lorenzo, E. D., ... Smith, C. A. (2016, jun). The pacific decadal oscillation, revisited. *Journal of Climate*, *29*(12), 4399–4427. Retrieved from https://doi.org/10.1175%2Fjcli-d-15-0508.1 doi: 10.1175/jcli-d-15-0508.1

Phillips, A. S., Deser, C., & Fasullo, J. (2014). [software] a new tool for evaluating modes of variability in climate models. *EOS*, *95*, 453–455. Retrieved from https://www.cesm.ucar.edu/working_groups/CVC/cvdp/ doi: 10.1002/2014EO490002

Pinto, J. G., Reyers, M., & Ulbrich, U. (2010, mar). The variable link between PNA and NAO in observations and in multi-century CGCM simulations. *Climate Dynamics*, *36*(1-2), 337–354. Retrieved from https://doi.org/10.1007%2Fs00382-010-0770-x doi: 10.1007/s00382-010-0770-x

Power, S., Casey, T., Folland, C., Colman, A., & Mehta, V. (1999, may). Inter-decadal modulation of the impact of ENSO on australia. *Climate Dynamics*, *15*(5), 319–324. Retrieved from https://doi.org/10.1007%2Fs003820050284 doi: 10.1007/s003820050284

Qiu, B., Schneider, N., & Chen, S. (2007, jul). Coupled decadal variability in the north pacific: An observationally constrained idealized model∗.*Journal of Climate*, *20*(14), 3602 − −3620.*Retrievedfrom* doi: 10.1175/jcli4190.1

Rohli, R. V., Snedden, G. A., Martin, E. R., & DeLong, K. L. (2022, aug). Impacts of ocean-atmosphere teleconnection patterns on the south-central united states. *Frontiers in Earth Science*, *10*. Retrieved from https://doi.org/10.3389%2Ffeart.2022.934654 doi: 10.3389/feart.2022.934654

Schneider, D. P., Deser, C., Fasullo, J., & Trenberth, K. E. (2013, mar). Climate data guide spurs discovery and understanding. *Eos, Transactions American Geophysical Union*, *94*(13), 121–122. Retrieved from https://doi.org/10.1002%2F2013eo130001 doi: 10.1002/2013eo130001

Shakun, J. D., & Shaman, J. (2009, oct). Tropical origins of north and south pacific decadal variability. *Geophysical Research Letters*, *36*(19). Retrieved from https://doi.org/10.1029%2F2009gl040313 doi: 10.1029/2009gl040313

Simon, A., Gastineau, G., Frankignoul, C., Lapin, V., & Ortega, P. (2022, aug). Pacific decadal oscillation modulates the arctic sea-ice loss influence on the midlatitude atmospheric circulation in winter. *Weather and Climate Dynamics*, *3*(3), 845–861. Retrieved from https://doi.org/10.5194%2Fwcd-3-845-2022 doi: 10.5194/wcd-3-845-2022

Stanhill, G., & Moreshet, S. (1992, may). Global radiation climate changes: The world network. *Climatic Change*, *21*(1), 57–75. Retrieved from https://doi.org/10.1007%2Fbf00143253 doi: 10.1007/bf00143253

Stephens, G. L., O'Brien, D., Webster, P. J., Pilewski, P., Kato, S., & lin Li, J. (2015, mar). The albedo of earth. *Reviews of Geophysics*, *53*(1), 141–163. Retrieved from https://doi.org/10.1002%2F2014rg000449 doi: 10.1002/2014rg000449

Student. (1908, 03). The probable error of a mean. *Biometrika*, *6*(1), 1-25. Retrieved from https://doi.org/10.1093/biomet/6.1.1 doi: 10.1093/biomet/6.1.1

Taguchi, B., Xie, S.-P., Schneider, N., Nonaka, M., Sasaki, H., & Sasai, Y. (2007, jun). Decadal variability of the kuroshio extension: Observations and an eddy-resolving model hindcast∗. *Journal of Climate*, *20*(11), 2357 − −2377. *Retrievedfrom* doi: 10.1175/jcli4142.1

Trenberth, K. E., & Fasullo, J. T. (2009, apr). Global warming due to increasing absorbed solar radiation. *Geophysical Research Letters*, *36*(7), n/a–n/a. Retrieved from https://doi.org/10.1029%2F2009gl037527 doi: 10.1029/2009gl037527

van den Dool, H. M., Saha, S., & Johansson, Å. (2000, April). Empirical orthogonal teleconnections. *Journal of Climate*, *13*(8), 1421–1435. Retrieved from https://doi.org/10.1175/1520-0442(2000)013<1421:eot>2.0.co;2 doi: 10.1175/1520-0442(2000)013⟨1421:eot⟩2.0.co;2

Welch, P. (1967, jun). The use of fast fourier transform for the estimation of power spectra: A method based on time averaging over short, modified periodograms. *IEEE Transactions on Audio and Electroacoustics*, *15*(2), 70–73. Retrieved from https://doi.org/10.1109%2Ftau.1967.1161901 doi: 10.1109/tau.1967.1161901

Wild, M. (2009, June). Global dimming and brightening: A review. *Journal of Geophysical Research*, *114*. Retrieved from https://doi.org/10.1029/2008jd011470 doi: 10.1029/2008jd011470

Wild, M., Folini, D., Hakuba, M. Z., Schär, C., Seneviratne, S. I., Kato, S., ... König-Langlo, G. (2014, dec). The energy balance over land and oceans: an assessment based on direct observations and CMIP5 climate models. *Clim Dyn*, *44*(11-12), 3393–3429. Retrieved from https://doi.org/10.1007%2Fs00382-014-2430-z doi: 10.1007/s00382-014-2430-z

Wild, M., Folini, D., Schär, C., Loeb, N., Dutton, E. G., & König-Langlo, G. (2012, nov). The global energy balance from a surface perspective. *Climate Dynamics*, *40*(11-12), 3107–3134. Retrieved from https://doi.org/10.1007%2Fs00382-012-1569-8 doi: 10.1007/s00382-012-1569-8

Wills, R. C. J., Armour, K. C., Battisti, D. S., Proistosescu, C., & Parsons, L. A. (2021, November). Slow modes of global temperature variability and their impact on climate sensitivity estimates. *Journal of Climate*, *34*(21), 8717–8738. Retrieved from https://doi.org/10.1175/jcli-d-20-1013.1 doi: 10.1175/jcli-d-20-1013.1

Wills, R. C. J., Battisti, D. S., Proistosescu, C., Thompson, L., Hartmann, D. L., & Armour, K. C. (2019, feb). Ocean circulation signatures of north pacific decadal variability. *Geophysical Research Letters*, *46*(3), 1690–1701. Retrieved from https://doi.org/10.1029%2F2018gl080716 doi: 10.1029/2018gl080716

Zhang, Y., Xie, S.-P., Kosaka, Y., & Yang, J.-C. (2018, oct). Pacific decadal oscillation: Tropical pacific forcing versus internal variability. *Journal of Climate*, *31*(20), 8265–

8279. Retrieved from https://doi.org/10.1175%2Fjcli-d-18-0164.1 doi: 10.1175/jcli-d-18-0164.1

Zheng, Z. (2021, February). *zzheng93/pyeof: First release.* Zenodo. Retrieved from https://doi.org/10.5281/zenodo.4556051 doi: 10.5281/zenodo.4556051